Article

Cancer Cell

Integrated Molecular and Clinical Analysis of 1,000 Pediatric Low-Grade Gliomas

Graphical Abstract

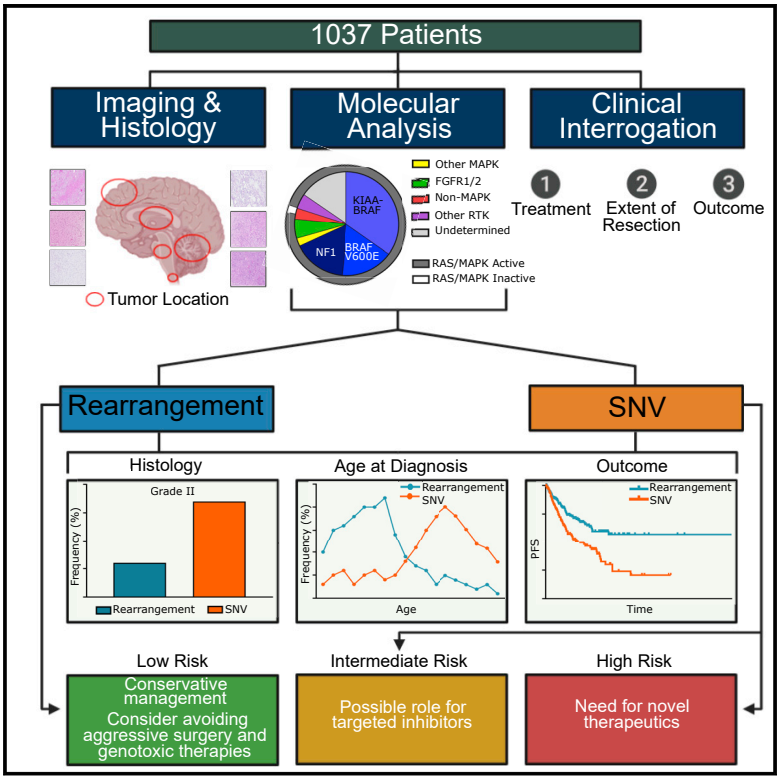

Highlights

- *KIAA1549-BRAF*, BRAF p.V600E, and NF1 mutations account for 2/3 of pLGG
- Activation of the RAS/MAPK pathway is nearly universal in pLGG
- pLGG comprise two distinct clinical subgroups: rearrangement- or SNV-driven
- Risk stratification based on alteration type effectively predicts patient outcome

Authors

Scott Ryall, Michal Zapotocky, Kohei Fukuoka, ..., David W. Ellison, Uri Tabori, Cynthia Hawkins

Correspondence

cynthia.hawkins@sickkids.ca

In Brief

Ryall et al. perform a comprehensive analysis of the molecular underpinnings and clinical correlates of 1000 pediatric low-grade gliomas. They uncover unique clinical features based on the type of molecular alteration identified and provide a risk based stratification to help infer treatment decisions.

Ryall et al., 2020, Cancer Cell *37*, 569–583
April 13, 2020
https://doi.org/10.1016/j.ccell.2020.03.011

CellPress

Cancer Cell
Article

Integrated Molecular and Clinical Analysis of 1,000 Pediatric Low-Grade Gliomas

Scott Ryall,[1,2,27] Michal Zapotocky,[1,3,4,27] Kohei Fukuoka,[1,3] Liana Nobre,[1,3] Ana Guerreiro Stucklin,[1,3,5] Julie Bennett,[1,3] Robert Siddaway,[1] Christopher Li,[1,2] Sanja Pajovic,[1] Anthony Arnoldo,[6] Paul E. Kowalski,[6] Monique Johnson,[6] Javal Sheth,[1,6] Alvaro Lassaletta,[1,3,7] Ruth G. Tatevossian,[8] Wilda Orisme,[8] Ibrahim Qaddoumi,[9] Lea F. Surrey,[10,11] Marilyn M. Li,[10] Angela J. Waanders,[11,12,13,14] Stephen Gilheeney,[15] Marc Rosenblum,[16] Tejus Bale,[16] Derek S. Tsang,[17,18] Normand Laperriere,[17,18] Abhaya Kulkarni,[19,20] George M. Ibrahim,[19,20] James Drake,[19,20]

(Author list continued on next page)

[1]Arthur and Sonia Labatt Brain Tumour Research Centre, The Hospital for Sick Children, 555 University Avenue, Toronto, ON M5G 1X8, Canada
[2]Department of Laboratory Medicine and Pathobiology, University of Toronto, Toronto, ON, Canada
[3]Department of Haematology/Oncology, The Hospital for Sick Children, Toronto, ON, Canada
[4]Second Faculty of Medicine, Charles University and University Hospital Motol, Prague, Czech Republic
[5]Children's Research Center, University Children's Hospital Zurich, Zurich, Switzerland
[6]Department of Paediatric Laboratory Medicine, The Hospital for Sick Children, Toronto, ON, Canada
[7]Department of Pediatric Hematology and Oncology, Hospital Universitario Niño Jesús, Madrid, Spain
[8]Department of Pathology, St. Jude Children's Research Hospital, Memphis, TN, USA
[9]Department of Oncology, St. Jude Children's Research Hospital, Memphis, TN, USA
[10]Department of Pathology and Laboratory Medicine, Children's Hospital of Philadelphia, Philadelphia, PA, USA
[11]Department of Genomic Diagnostics, Children's Hospital of Philadelphia, Philadelphia, PA, USA
[12]Center for Data Driven Discovery in Biomedicine, Children's Hospital of Philadelphia, Philadelphia, PA, USA
[13]Department of Hematology, Oncology, and Stem Cell Transplant, Ann & Robert H Lurie Children's Hospital of Chicago, Chicago, IL, USA
[14]Department of Pediatrics, Feinberg School of Medicine Northwestern University, Chicago, IL, USA
[15]Department of Pediatrics, Memorial Sloan Kettering Cancer Center, New York, NY, USA

(Affiliations continued on next page)

SUMMARY

Pediatric low-grade gliomas (pLGG) are frequently driven by genetic alterations in the RAS-mitogen-activated protein kinase (RAS/MAPK) pathway yet show unexplained variability in their clinical outcome. To address this, we characterized a cohort of >1,000 clinically annotated pLGG. Eighty-four percent of cases harbored a driver alteration, while those without an identified alteration also often exhibited upregulation of the RAS/MAPK pathway. pLGG could be broadly classified based on their alteration type. Rearrangement-driven tumors were diagnosed at a younger age, enriched for WHO grade I histology, infrequently progressed, and rarely resulted in death as compared with SNV-driven tumors. Further sub-classification of clinical-molecular correlates stratified pLGG into risk categories. These data highlight the biological and clinical differences between pLGG subtypes and opens avenues for future treatment refinement.

INTRODUCTION

Pediatric low-grade gliomas (pLGG) are the most frequent brain tumors in children, accounting for approximately 30% of all cases (Ostrom et al., 2015). pLGG encompass a broad range of glial, neuronal, and mixed glioneuronal entities in the World Health Organization (WHO) classification of central nervous system (CNS) tumors (Louis et al., 2016). Unlike lower-grade gliomas in adults,

Significance

Pediatric low-grade gliomas (pLGG) are the most common brain tumors affecting children. This integrated clinicopathologic and genomic analysis of >1,000 pLGG defines molecular subgroups with distinct biological drivers and clinical features. RAS/MAPK pathway is activated near universally in pLGG, regardless of the presence of a clear genomic activator. Further, although many alterations converge on the RAS/MAPK pathway, clinical presentation and outcome are highly variable depending on the type of underlying alteration. This information helped define clinical risk groups of pLGG with different progression-free and overall survival which likely require different treatment strategies. As modernized treatment regimens utilize alteration-specific agents, we provide the framework for molecular classification of pLGG reflecting unique biological mechanisms driving the disease that likely promote different therapeutic susceptibilities.

Peter Dirks,[1,2,20] Michael D. Taylor,[1,2,20] James T. Rutka,[1,2,20] Suzanne Laughlin,[21,22] Manohar Shroff,[21,22] Mary Shago,[2,6] Lili-Naz Hazrati,[2,23] Colleen D'Arcy,[2,23,24] Vijay Ramaswamy,[1,3,25] Ute Bartels,[3,25] Annie Huang,[1,2,3] Eric Bouffet,[3,25] Matthias A. Karajannis,[15] Mariarita Santi,[10,11] David W. Ellison,[8] Uri Tabori,[1,3,26,28] and Cynthia Hawkins[1,2,23,29,*]

[16]Department of Pathology, Memorial Sloan Kettering Cancer Center, New York, NY, USA
[17]Radiation Medicine Program, Princess Margaret Cancer Centre, University Health Network, Toronto, ON, Canada
[18]Department of Radiation Oncology, Faculty of Medicine, University of Toronto, Toronto, ON, Canada
[19]Department of Surgery, University of Toronto, Toronto, ON, Canada
[20]Department of Neurosurgery, The Hospital for Sick Children, Toronto ON, Canada
[21]Department of Radiology, The Hospital for Sick Children, Toronto ON, Canada
[22]Department of Medical Imaging, University of Toronto, Toronto, ON, Canada
[23]Department of Pathology, The Hospital for Sick Children, Toronto, ON, Canada
[24]Department of Anatomical Pathology, The Alfred Hospital, Prahran, VIC, Australia
[25]Department of Paediatrics, University of Toronto, Toronto, ON, Canada
[26]Department of Medical Biophysics, University of Toronto, Toronto, ON, Canada
[27]These authors contributed equally
[28]Co-senior authors
[29]Lead Contact
*Correspondence: cynthia.hawkins@sickkids.ca
https://doi.org/10.1016/j.ccell.2020.03.011

which primarily arise in the cerebral hemispheres and inevitably transform to higher-grade glioma, pLGG can occur throughout the CNS and rarely transform (Broniscer et al., 2007; Mistry et al., 2015). Nevertheless, outcome and response to therapy is highly variable. If complete surgical resection is successful, 10-year progression-free survival (PFS) exceeds 85%, but drops below 50% if there is radiologically visible residual tumor (Wisoff et al., 2011). In deep-seated midline locations, gross total resection (GTR) is not often achievable and adjuvant therapy may be required, often with unsatisfactory tumor control and/or long-term morbidity (Krishnatry et al., 2016; Nageswara and Packer, 2014). Which patients require these therapies and who will benefit from them is not yet well understood.

Over the last decade, molecular profiling studies have incrementally identified key genetic events in pLGG that converge on the RAS-mitogen-activated protein kinase (RAS/MAPK) pathway. Most commonly, these are somatic events involving *BRAF* or germline *NF1* alterations (Collins et al., 2015; Jones et al., 2008; Schindler et al., 2011; Dougherty et al., 2010; Lassaletta et al., 2017; Listernick et al., 1999; Uusitalo et al., 2016; Seminog and Goldacre, 2013). In addition to these common pLGG alterations, rarer alterations affecting RAS/MAPK signaling, including those involving *FGFR1/2/3*, *NTRK2*, *RAF1*, *ALK*, and *ROS1* (Zhang et al., 2013; Jones et al., 2013; Qaddoumi et al., 2016; Guerreiro Stucklin et al., 2019), as well as non-RAS/MAPK alterations, such as *MYB*, *MYBL1*, *IDH1*, and *H3F3A* (Qaddoumi et al., 2016; Tatevossian et al., 2010; Ramkissoon et al., 2013; Bandopadhayay et al., 2016; Ryall et al., 2016; Hartmann et al., 2009) have been identified in small numbers of cases. However, several key issues remain undefined: (1) Are all *NF1*, *BRAF* fused and *BRAF* mutant tumors the same? (2) What is the mechanism of tumorigenesis in pLGG without an identifiable genetic alteration? (3) What are the clinical features of the rare alterations in pLGG and is their outcome unique? (4) Can molecular alterations help provide biological insights for disease stratification?

To answer these questions and provide a population-based resource for the pediatric neuro-oncology community, we molecularly characterized >1,000 pLGG with comprehensive clinical data. This enabled us to provide a statistically robust, annotated resource which includes representation of the rarest pLGG molecular entities and their clinical features.

RESULTS

Patient Cohort

Our population-based cohort of pLGG consisted of 976 patients (<19 years) followed and treated at the Hospital for Sick Children (Toronto, ON, Canada) from 1986 to 2017 (Table S1). For each patient we collected demographic, treatment and outcome data.

At the population level, tumors were distributed equally between the diencephalon (n = 313, 32%; n = 124, 13% were from neurofibromatosis type 1 [NF1] patients), cerebral hemispheres (n = 265, 27%), and the cerebellum (n = 252, 26%), whereas pure brainstem (n = 92, 9.4%), spinal cord (n = 41, 4.2%), and extensively disseminated tumors (n = 13, 1.3%) were less frequent (Figure 1A). Upon pathologic review of non-NF1 cases (n = 843), pilocytic astrocytoma (n = 303, 36%) was the most common diagnosis (excluding LGG, not otherwise specified [NOS]) across tumor locations (Figure 1B) with the exception of the cerebral hemispheres, which was histologically diverse (Figure 1C). The median age of diagnosis was 7.6 years (range 0–18.7 years), with pLGG in the cerebral hemispheres being diagnosed at a later age (median = 10.7 years) as compared with other tumor locations ($p < 0.0001$, ANOVA; all pairwise comparisons adjusted $p < 0.0001$, t test) (Figure 1D). There was a significant association between tumor location, PFS, and overall survival (OS) ($p < 0.0001$, log rank test) (Figures 1E and S1), with 10-year PFS and OS best for patients with tumors in the cerebellum (89% and 99%, respectively), and worst for those with extensively disseminated disease (0% and 67%, respectively). Importantly, only 7.5% of patients succumbed to their disease (median time to death = 3.9 years, median OS follow-up = 15.9 years) despite 33% experiencing tumor progression (median time to progression = 2.3 years, median PFS follow-up = 5.9 years) (Figure 1F).

Characteristics of NF1-Driven pLGG

Patients with the genetic pre-disposition disorder NF1 are diagnosed using a series of clinical observations and tests indicative

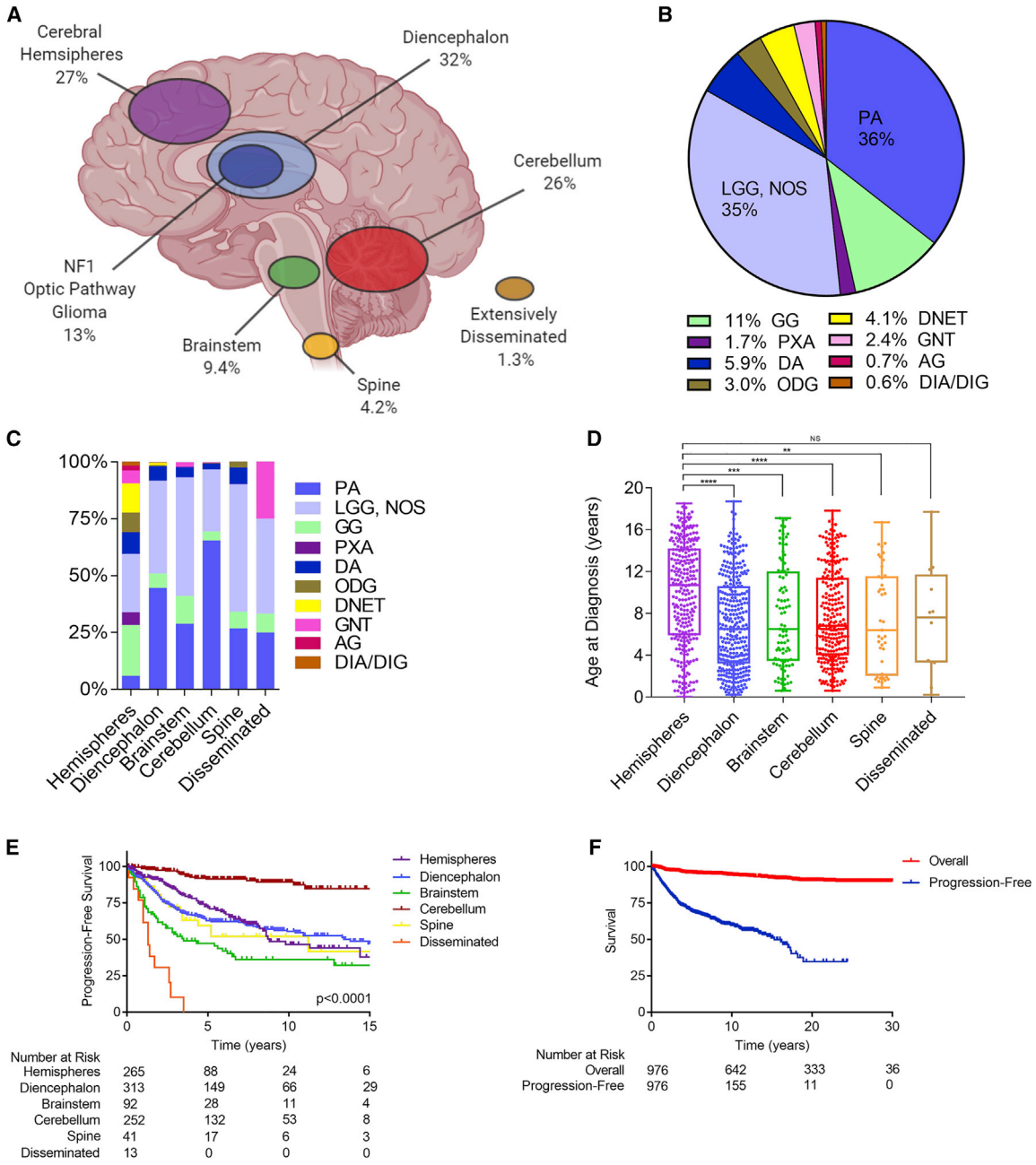

Figure 1. pLGG Cohort Details

(A) Anatomical location of all pLGG within the cohort (n = 976).

(B) The histological spectrum of all non-NF1 pLGG (n = 843). PA, pilocytic astrocytoma; LGG, NOS, low-grade glioma, not otherwise specified; GG, ganglioglioma; DNET, dysembryoplastic neuroepithelial tumor; PXA, pleomorphic xanthoastrocytoma; GNT, glioneuronal tumor; DA, diffuse astrocytoma; AG, angiocentric glioma; ODG, oligodendroglioma; DIA/DIG, desmoplastic infantile astrocytoma/ganglioglioma.

(C) Histological distribution of samples based on tumor location of all non-NF1 pLGG (n = 843).

(D) Boxplot showing age at diagnosis separated by tumor location of the entire pLGG cohort (n = 976). The thick line within the box represents the median, the lower and upper limits of the box represent the first and third quartiles and the whiskers the minimum and maximum values. Adjusted p value for all pairwise comparisons, t test. *p < 0.05, **p < 0.01, ***p < 0.001, ****p < 0.0001; n.s., not significant.

(E) Progression-free survival of the pLGG cohort segregated by tumor location. p Value calculated via the log rank test.

(F) Progression-free and overall survival of the entire pLGG cohort (n = 976). p value calculated via the log rank test.

See also Figure S1 and Table S1.

of a germline *NF1* mutation (Gutmann et al., 2017). Therefore, pLGG arising in these patients are primarily diagnosed via imaging and clinical observation, rather than their genetics. Therefore, we examined this group of tumors separately, before our extensive molecular profiling of somatic pLGG (Table S2).

Although NF1-driven pLGG are generally thought to have a favorable clinical course, analysis of a large cohort revealed important risk groups. In our study, NF1-driven pLGG accounted for 14% of cases (n = 133). Although most NF1 pLGG occur as optic pathway glioma (OPG), 19% (n = 25) arose outside of this location. Patients with NF1 tumors arising outside the optic pathway had significantly worse OS and PFS compared with those arising in the optic pathway (p = 0.0011, p = 0.0029, respectively, log rank test) (Figures S2A and S2B). Furthermore, of the high risk, recurrent, and biopsied NF1 pLGG, 20% were found to harbor mutations in other molecular drivers, including BRAF p.V600E, *FGFR1*, and/or *H3F3A* (H3.3) p.K27M. All of these patients experienced multiple progressions with two succumbing to their disease post-chemoradiation after 15.5 and 13.7 years, respectively. These observations, although preliminary, suggest that non-OPG NF1 tumors may require specialized management, including an early biopsy and molecular profiling in agreement with recent reports (D'Angelo et al., 2019).

The Molecular Landscape of Non-NF1 pLGG

To determine the true frequency of molecular alterations in pLGG we analyzed 540 tumors from 2000 to 2017 where material quality was sufficient to utilize our tiered profiling approach (Figure S3A). In total, 88% (n = 477/540) had sufficient material for molecular profiling.

Together, *KIAA1549-BRAF* (n = 166), BRAF p.V600E (n = 79), and germline *NF1* mutations (n = 79) accounted for 68% (n = 324) of tumors (Figures 2A–2C). Rare alterations accounted for an additional 17% of cases. These included non-canonical *BRAF* alterations, such as fusions partnered with genes others than *KIAA1549* (n = 4), 2 insertion events at position 600 (p.V600ins) and 1 SNV at position 594 (p.D594N) (Figures 2A–2C and 2E). A further 1.3% (n = 6) of cases contained alterations in other direct members of the RAS/MAPK pathway, including three *RAF1* fusions, two *KRAS* mutations, and one patient with a short deletion in *MAP2K1* (Figures 2A–2C and 2E). The next most frequent alterations were those affecting receptor tyrosine kinases (RTKs) (n = 45, 9.4%) (Figures 2A–2C) and included two categories: *FGFR* and other RTKs. Alterations in *FGFR* most frequently involved *FGFR1/2* (n = 29, 6.1%) and included *FGFR1-TACC1* fusions (n = 7, 1.5%), *FGFR1* tyrosine kinase domain (TKD) duplications (n = 10, 2.1%), *FGFR2* fusions (n = 5, 1.0%), and hotspot mutations in *FGFR1* (n = 7, 1.5%) (Figures 2A–2C). Alterations in other RTKs (n = 16, 3.4%) included mutations in *MET* (n = 5, 1.0%) or *PDGFRA* (n = 1, 0.2%), as well as fusions involving *ALK* (n = 2, 0.4%), *ROS1* (n = 2, 0.4%), and *NTRK2* (n = 2, 0.4%) (Figures 2A–2C and 2E). Finally, 4.6% (n = 22) of cases contained alterations in genes with seemingly no direct impact on the RAS/MAPK pathway (Figures 2A–2C). These included mutations in *H3F3A* (n = 4, 0.8%), *IDH1* (n = 4, 0.8%), and rearrangements involving *MYB* (n = 6, 1.3%) or *MYBL1* (n = 5, 1.0%) (Figures 2A–2C). Altogether, we identified a driver mutation in 84% of pLGG. Incidences of molecular alterations excluding NF1 patients (n = 397) are seen in Figures 2B and 2D and enrichment across tumor locations and pathologies in Figures S3B and S3C.

The RAS/MAPK Pathway Is Upregulated across pLGG Regardless of Underlying Mutation

The predilection of NF1 patients for developing pLGG together with the identification of *KIAA1549-BRAF* and BRAF p.V600E as molecular drivers in pLGG led to the hypothesis that upregulation of the RAS/MAPK pathway may be the primary driver for tumor formation (Collins et al., 2015; Northcott et al., 2015; Jones et al., 2012; Zhang et al., 2013). However, how broadly this applies to pLGG has not been tested and is of major importance due to the increasing use of the RAS/MAPK pathway-targeting agents in the clinic.

We therefore asked whether the 16% of pLGG without identified mutations nonetheless resulted in upregulation of the RAS/MAPK pathway. To test this hypothesis, we first analyzed a series of pLGG with non-*BRAF* alterations, including *FGFR* alterations, rare RTKs, *RAF1* fusions, *KRAS* mutations, and *MYB* or *MYBL1* rearrangements and compared their phosphorylated ERK (ppERK) levels with *KIAA1549-BRAF* and BRAF p.V600E tumors. Interestingly, all tumors had significantly increased ppERK as compared with normal brain controls ($p < 0.0001$, ANOVA; all pairwise comparisons adjusted $p < 0.0001$, t test) (Figure 3A). Importantly, increased ppERK was also seen in *MYB*- and *MYBL1*-altered tumors, which would not themselves be expected to directly signal via the RAS/MAPK pathway. To further explore whether RAS/MAPK pathway upregulation is a unifying event in pLGG even in the absence of an activating genetic event, we examined a subset of pLGG in which a molecular driver was not identified. Utilizing RNA sequencing, we performed single sample gene set enrichment analysis (ssGSEA) focusing on the RAS/MAPK pathway. We observed that genes known to be up- or downregulated by RAS/MAPK activation were significantly enriched in these tumors as compared with normal brain controls (Figures 3B and 3C). Furthermore, when compared against samples with known RAS/MAPK pathway alterations, the activation signature was indiscernible between the two ($p = 0.4103$, ANOVA; all pairwise comparisons adjusted $p < 0.0001$, t test) (Figure 3D), indicating similar levels of RAS/MAPK upregulation in pLGG lacking a clear molecular driver.

Alteration Type Predicts pLGG Outcome

To further interrogate the impact of rare pLGG alterations, we collected data from an additional 61 patients in whom a rare molecular alteration had been previously identified from St. Jude Children's Hospital (Memphis, TN, USA), Children's Hospital of Philadelphia (Philadelphia, PA, USA), and Memorial Sloan Kettering Cancer Center (New York, NY, USA) (Table S3). This yielded a total of 1,037 pLGG. With these additional cases and detailed clinical and molecular information, we asked which features were predictive of clinical outcome in pLGG. Interestingly, patient outcome was significantly associated with the type of alteration (rearrangement versus SNV), and not exclusively on which particular gene was altered (Figures 4A and 4B; Table 1). Patients with rearrangement-driven pLGG had good long-term outcome with very few deaths (n = 7, 2.6%) and fewer progressions (n = 67, 27%) (Figures 4B–4D; Table 1). In contrast, patients with SNV-driven

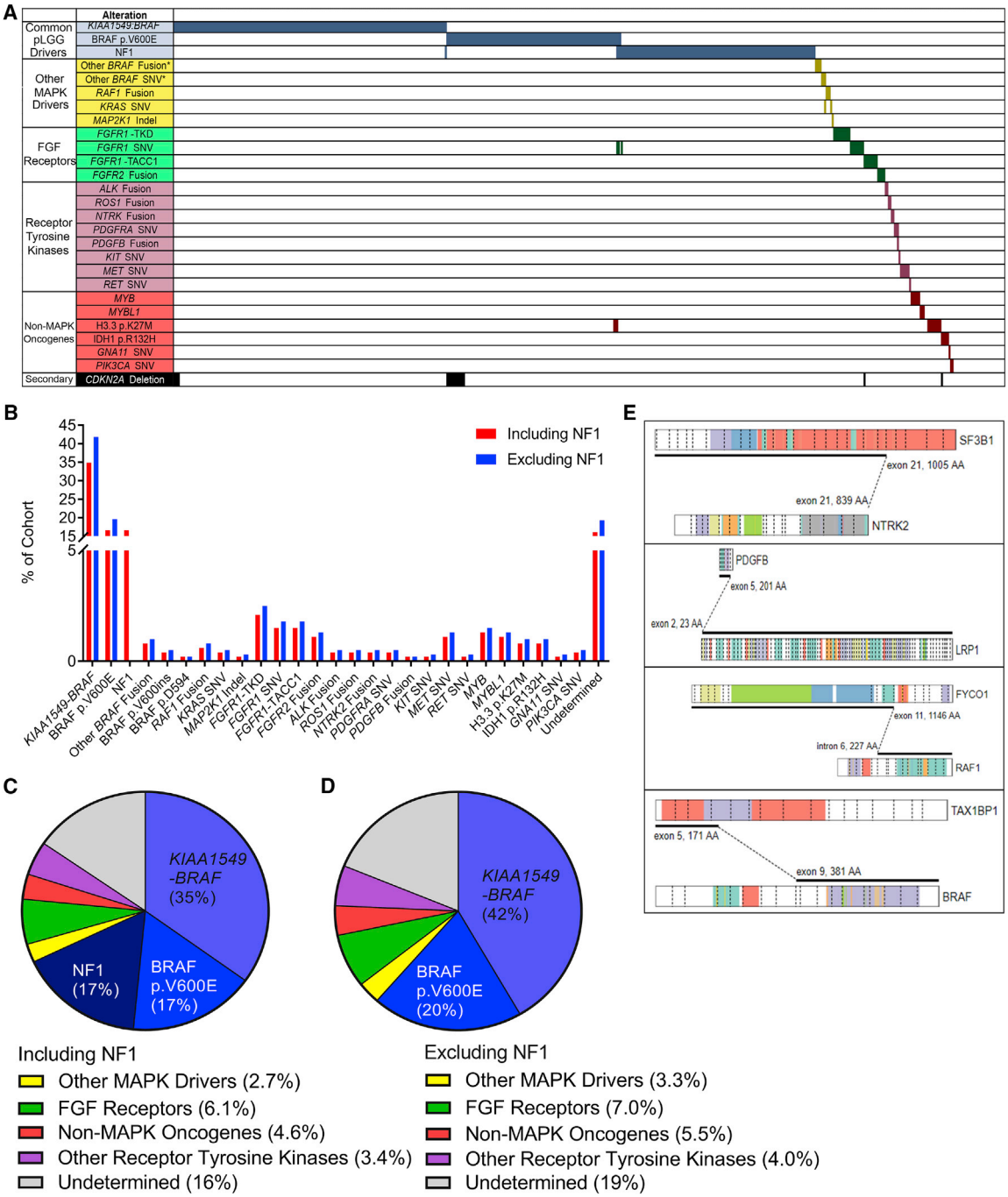

Figure 2. The Molecular Landscape of pLGG

(A) Oncoprint representation of the molecular alterations and their associated categories in 610 pLGG. Samples are arranged in columns with genes and gene categories labeled along the row. *Denotes that these BRAF SNVs and fusions are not the canonical *KIAA1549-BRAF* or p.V600E.

(B) Bar graph of all recurrent somatic mutations across all 477 cases diagnosed from 2000 to 2017 for which sufficient material for molecular testing was available, in order of frequency and colored based on the inclusion (blue) or exclusion (red) of NF1 patients.

(C) Pie chart depicting the frequency of alterations per molecular category in a population-based cohort of pLGG diagnosed from 2000 to 2017 (n = 477).

(D) Pie chart depicting the frequency of alterations per molecular category in non-NF1 pLGG diagnosed from 2000 to 2017 (n = 397).

(E) Schematic representation of the rare and novel fusions identified in this study. Figures were derived using the Protein Paint feature of the St. Jude PeCan website (https://pecan.stjude.cloud/proteinpaint).

See also Figures S2 and S3 and Table S2.

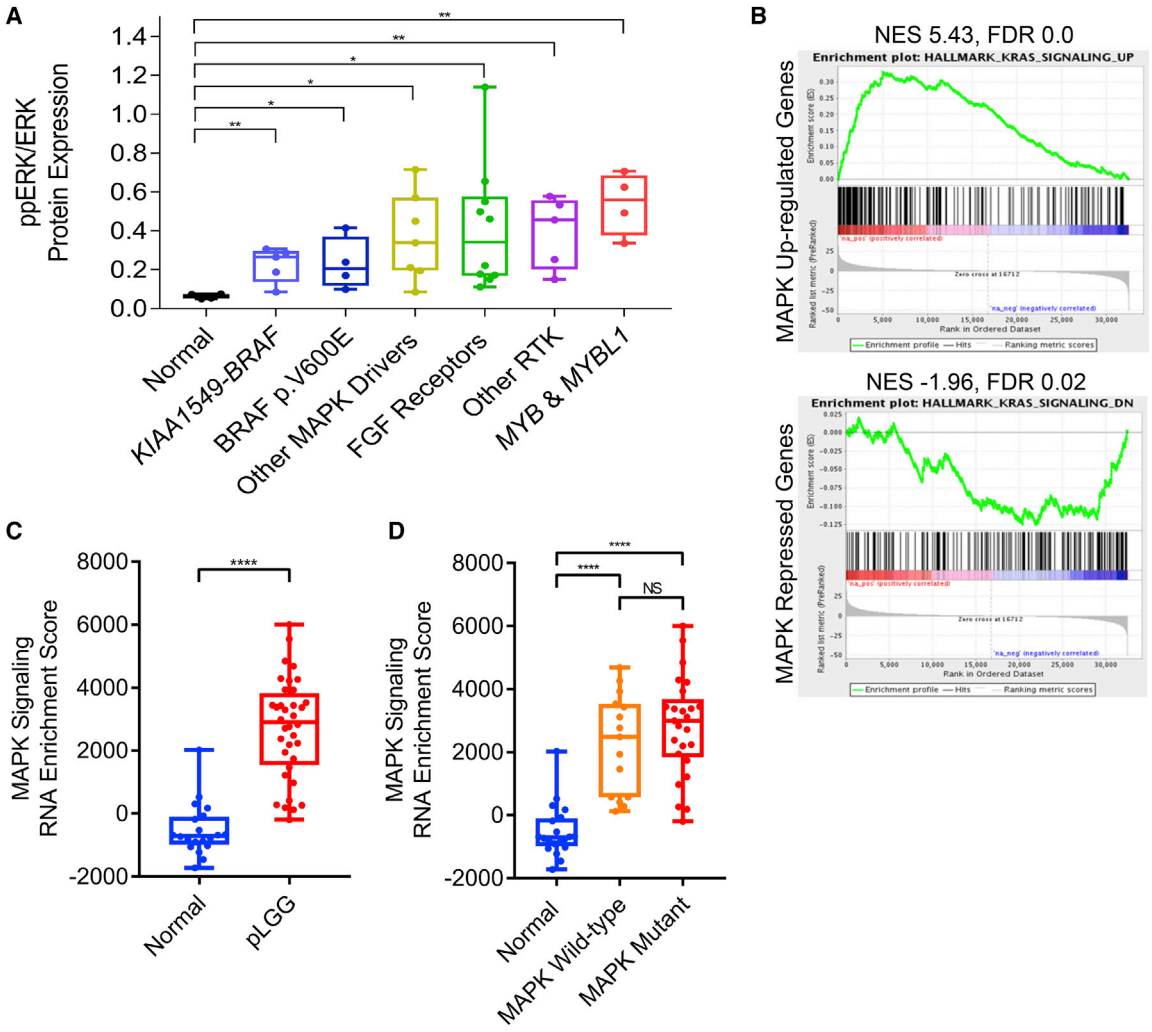

Figure 3. RAS/MAPK Pathway Upregulation in Non-canonical and Molecularly Undetermined pLGG

(A) Boxplot showing the ppERK/ERK protein levels, separated by molecular alteration. The thick line within the box represents the median, the lower and upper limits of the box represent the first and third quartiles and the whiskers the minimum and maximum values. Adjusted p value for all pairwise comparisons, t test.*p < 0.05, **p < 0.01, ***p < 0.001, ****p < 0.0001; n.s., not significant.

(B) Pre-ranked gene set enrichment analysis (GSEA) of the RAS/MAPK pathway activation signature in molecularly undetermined pLGG. NES, normalized enrichment score; FDR, false-discovery rate.

(C) Single sample gene set enrichment analysis (ssGSEA) of RAS/MAPK activation for normal brain controls and molecularly undetermined pLGG. The thick line within the box represents the median, the lower and upper limits of the box represent the first and third quartiles and the whiskers the minimum and maximum values. Adjusted p value for all pairwise comparisons, Mann-Whitney test. *p < 0.05, **p < 0.01, ***p < 0.001, ****p < 0.0001; n.s., not significant.

(D) RAS/MAPK ssGSEA scores for known RAS/MAPK mutant and molecularly undetermined pLGG compared with normal brain. The thick line within the box represents the median, the lower and upper limits of the box represent the first and third quartiles and the whiskers the minimum and maximum values. Adjusted p value for all pairwise comparisons, t test.*p < 0.05, **p < 0.01, ***p < 0.001, ****p < 0.0001; n.s., not significant.

pLGG were significantly more likely to succumb to their disease (n = 24, 13%, p < 0.0001, Fisher's exact test versus rearrangement-driven) and/or progress (n = 80, 44%, p < 0.0001, Fisher's exact test versus fusion-driven) (Table 1; Figures 4B–4D). Furthermore, rearrangement-driven pLGG were diagnosed at a significantly younger age (median 6.6 versus 10.9 years, p < 0.0001, t test) and were enriched for WHO grade I histology (p < 0.0001, Fisher's exact test) (Figure 4B; Table 1). This pattern is evident in *BRAF*, where tumors with *KIAA1549-BRAF* have superior outcome to BRAF p.V600E (5-year PFS of 69% for *KIAA1549-BRAF* versus 52% for BRAF p.V600E, p = 0.0058, log rank test). When investigating *BRAF* in grade I tumors alone, the pattern remained (5-year PFS of 72% and 56% for *KIAA1549-BRAF* and BRAF p.V600E, respectively, p = 0.0176). Although the numbers are too small to allow statistical comparisons between SNVs and fusions for other genes, the same trend is evident. For example, for *FGFR1*, patients with *FGFR1-TACC1* or *FGFR1* TKD tumors had similar outcome to those with *KIAA1549-BRAF* fusions (5-year PFS of 69% for all). Patients with *FGFR1* SNVs, on the other hand, were more similar to BRAF p.V600E (5-year PFS of 53% and 52% for *FGFR1* SNV and BRAF p.V600E,

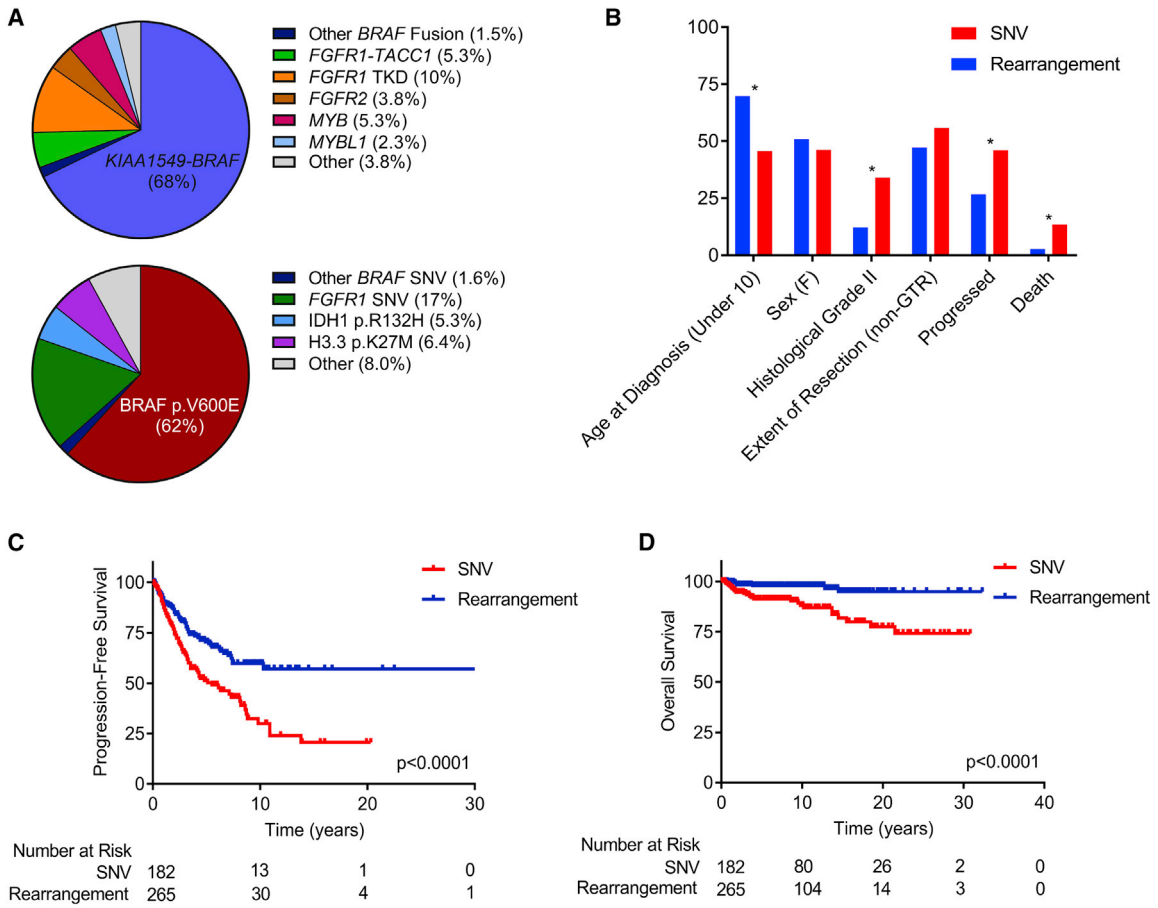

Figure 4. Rearrangement versus SNV-Driven pLGG

(A) Pie charts depicting the molecular alteration breakdown of rearrangement- (top) (n = 265) and SNV -driven (bottom) (n = 182) pLGG.

(B) Rearrangement- versus SNV-driven pLGG as compared across several clinical features. *Adjusted $p < 0.05$, Fisher's exact test. GTR, gross total resection.

(C) Kaplan-Meier plot of overall survival of cases separated by rearrangement- or SNV-driven status. p value calculated via the log rank test.

(D) Kaplan-Meier plot of progression-free survival of cases separated by rearrangement- or SNV-driven status. p value calculated via the log rank test.

See also Table S3.

respectively). Importantly, where *FGFR1-TACC1* and *FGFR1*-TKD tumors did not contain additional alterations, *FGFR1* SNVs often did, sometimes resulting in late deaths.

Characteristics of Fusion-Driven pLGG

BRAF *Fusions*

KIAA1549-BRAF was the most frequent alteration in pLGG (35%) and was almost exclusively a single-event driver (n = 175/180, 97%), with four cases also having a *CDKN2A* deletion and one present in a patient with NF1 (Figure 2A). These five rare cases are still alive (median follow-up = 7.5 years). *KIAA1549-BRAF* was significantly enriched in pilocytic astrocytoma (n = 150/180, 83%, $p < 0.0001$, Fisher's exact test), and in cerebellar tumors (n = 100/180, 56%, p = 0.0002, Fisher's exact test) (Figure 5A).

Because of the large number of tumors, we could sub-stratify the *BRAF* fusions into subgroups based on their breakpoints (Figure S4A). The most common *KIAA1549-BRAF* fusion involved exon 16 in *KIAA1549* and exon 9 in *BRAF* (16:09). Like all *KIAA1549-BRAF* fusions, 16:09 was significantly enriched in pilocytic astrocytoma (n = 73/83, 88%, $p < 0.0001$, Fisher's exact test) and in cerebellar tumors (n = 60/83, 72%, $p < 0.0001$, Fisher's exact test) (Figures S4B and S4C). Interestingly, the only *KIAA1549-BRAF* fusion seen in hemispheric tumors was 15:09 (Figure S4B). 15:09 was also the primary fusion seen in tumors with extensive dissemination (n = 5, 83%, $p < 0.0001$, Fisher's exact test). 15:09 fusions were associated with a worse PFS (p = 0.0003, log rank test, Figure S4D), with a 5-year PFS of 59% as compared with 77%–100% for other fusion subtypes. *BRAF* fusions not involving *KIAA1549* occurred exclusively in adolescents with no progression events (median follow-up = 3.7 years), while 15:11 was only observed in two infants who rapidly experienced tumor progression and died (Figures S4D and S4E). Identifying the specific fusion breakpoints of *KIAA1549-BRAF* will be important to properly ascertain their propensity for certain clinical features and impact on outcome.

FGFR1/2 *Fusions and* FGFR1 *TKD*

FGFR fusions/TKD were observed in 6.1% of the cohort (Figure 2B). *FGFR1-TACC1* pLGG were often cystic lesions, most commonly pilocytic astrocytoma (n = 7/14, 50%) and occurred

Table 1. Clinicopathologic Features of Rearrangement versus SNV-Driven pLGG

Characteristic	pLGG Subtype		
	Rearrangement	SNV	p Value
Number	265	182	
Grade			
I	216 (88)*	97 (66)*	<0.0001
II	30 (12)*	50 (34)*	
Sex			
Male	130 (49)	98 (54)	0.337
Female	135 (51)	84 (46)	
Age at Diagnosis			
Under 10 years	185 (70)	83 (46)	<0.0001
Over 10 years	80 (30)	99 (54)	
Mean	7.6 ± 4.8	10.1 ± 5.1	
Median	6.6 (0.5–18.9)	10.9 (0.2–18.9)	
Extent of Resection			
GTR	137 (52)	76 (44)	0.078
No GTR	127 (48)	96 (56)	
Location			
Cerebral hemisphere	86 (32)	97 (53)	<0.0001
Midline	75 (28)	72 (40)	
Cerebellum	104 (40)	13 (7)	
Progression			
Progressed	67 (27)	80 (46)	<0.0001
Stable	184 (73)	94 (54)	
5-year PFS	70.6	51.4	
10-year PFS	59.8	30.0	
Outcome			
Dead	7 (3)	24 (13)	<0.0001
Alive	249 (97)	155 (87)	
5-year OS	97.8	91.2	
10-year OS	97.8	88.1	

Values are displayed as raw counts and the percentage of the group. *Denotes categories with omitted samples (LGG, NOS was not assigned a histological grade). GTR, gross total resection; PFS, progression-free survival; OS, overall survival.
See also Tables S1 and S3.

throughout the CNS, most commonly in the cerebral hemispheres (n = 6/14, 43%) (Figure 5B). *FGFR1* TKD and *FGFR2* fused pLGG were primarily glioneuronal or oligodendroglial in origin, respectively and were restricted to the cerebral hemispheres (Figures 5C and 5D). *FGFR2* fusions included *FGFR2-INA*, *FGFR2-CTNNA3*, and *FGFR2-ERC1* (Figure S5). While progressions were seen in some cases (5-year PFS of 69%, 69%, and 88% for *FGFR1-TACC1*, *FGFR1* TKD, and *FGFR2* fused cases, respectively), none of these tumors resulted in patient death with a median follow-up of 11.3, 11.7, and 7.1 years, respectively (Figures 5B–5D).

ALK, ROS1, NTRK, *and* PDGFB *Fusions*

Fusions in other RTKs were rare in pLGG (3.4%) and included novel events as well as some previously described in pediatric gliomas (Wu et al., 2014; Aghajan et al., 2016; Kiehna et al., 2017; Guerreiro Stucklin et al., 2019). These included *CCDC88A-ALK*, *PPP1CB-ALK*, *GOPC-ROS1*, and *NTRK2-MID1* in addition to novel *NTRK2-SF3B1* and *PDGFB-LRP1* fusions (Figure 2E). These fusions were restricted to the cerebral hemispheres with the exception of the *ROS1* fusions, which were both seen in the intraventricular space (Table S4). Interestingly, *ALK* fusions were exclusively observed in infants (0.9 and 1.1 years). No patients harboring these alterations succumbed to their disease after a median follow-up of 4.9 years and only a single *ALK* and single *ROS1* fused patient progressed. A clinical summary of these rare fusions is included in Table S4.

MYB *and* MYBL1 *Rearrangements*

MYB and *MYBL1* alterations were histologically enriched for angiocentric glioma (n = 14, 100%, p < 0.0001, Fisher's exact test) and diffuse astrocytoma (n = 5, 83%, p < 0.0001, Fisher's exact test), respectively, with both primarily arising in the cerebral hemispheres (n = 13/14, 92% and n = 5/6, 83%, respectively, p < 0.0001, Fisher's exact test) (Figures 5E and 5F). All patients harboring either *MYB* or *MYBL1* rearrangements are alive with median follow-up of 8.1 and 5.3 years, respectively. However, while progressions were rare in *MYB*-altered tumors (n = 2/10, 20%), they were more frequent in those with *MYBL1* (n = 2/6, 33%), resulting in a 5-year PFS of 90% and 67%, respectively (Figures 5E and 5F). Our data suggest that the clinical differences between *MYB*- and *MYBL1*-altered tumors merit further investigation.

Characteristics of SNV-Driven pLGG

BRAF p.V600E

BRAF p.V600E was the second most common alteration in pLGG (17%) and was frequently associated with additional alterations, most commonly deletion of *CDKN2A* (n = 13, 9.6%) (Figure 2A). BRAF p.V600E also co-occurred with several other SNVs, including those in *NF1*, *FGFR1*, *KRAS*, and *H3F3A*, but never with a fusion event (Figure 2A). Unlike *KIAA1549-BRAF*, tumors with BRAF p.V600E were histologically diverse and included ganglioglioma (n = 36, 31%), diffuse astrocytoma (n = 16, 14%), and pleomorphic xanthoastrocytoma (n = 12, 10%) (Figure 6A). Both ganglioglioma and pleomorphic xanthoastrocytoma were more likely to harbor BRAF p.V600E than other tumor types (p = 0.0028, p = 0.0048, respectively, Fisher's exact test, Figure S3C). BRAF p.V600E cases occurred most frequently in the cerebral hemispheres (n = 64, 56%) but were also common in the diencephalon (n = 33, 29%) and, in contrast to *KIAA1549-BRAF*, were rare in the cerebellum (n = 6, 5.2%) (Figure 6A). BRAF p.V600E pLGG had worse OS and PFS than those with *KIAA1549-BRAF* (10-year OS 97% versus 89%, p = 0.0416 and 10-year PFS of 64% versus 30%, p = 0.0058, respectively, log rank test, Figures S6A and S6B). BRAF p.V600E tumors with pleomorphic xanthoastrocytoma histology had a worse outcome than those without (5-year PFS of 14% versus 58%, respectively, p = 0.0328, log rank test, Figure S6C), although OS was not significantly different (p = 0.1892, Figure S6D). The same was not the case for BRAF p.V600E tumors with co-occurring *CDKN2A* deletions (5-year PFS of 34% versus 55%, respectively, p = 0.1157, log rank test, Figure S6E), although OS was significantly different (p = 0.0100, log rank test, Figure S6F). However, both non-pleomorphic xanthoastrocytoma (5-year PFS of 55%) and *CDKN2A* balanced (5-year PFS

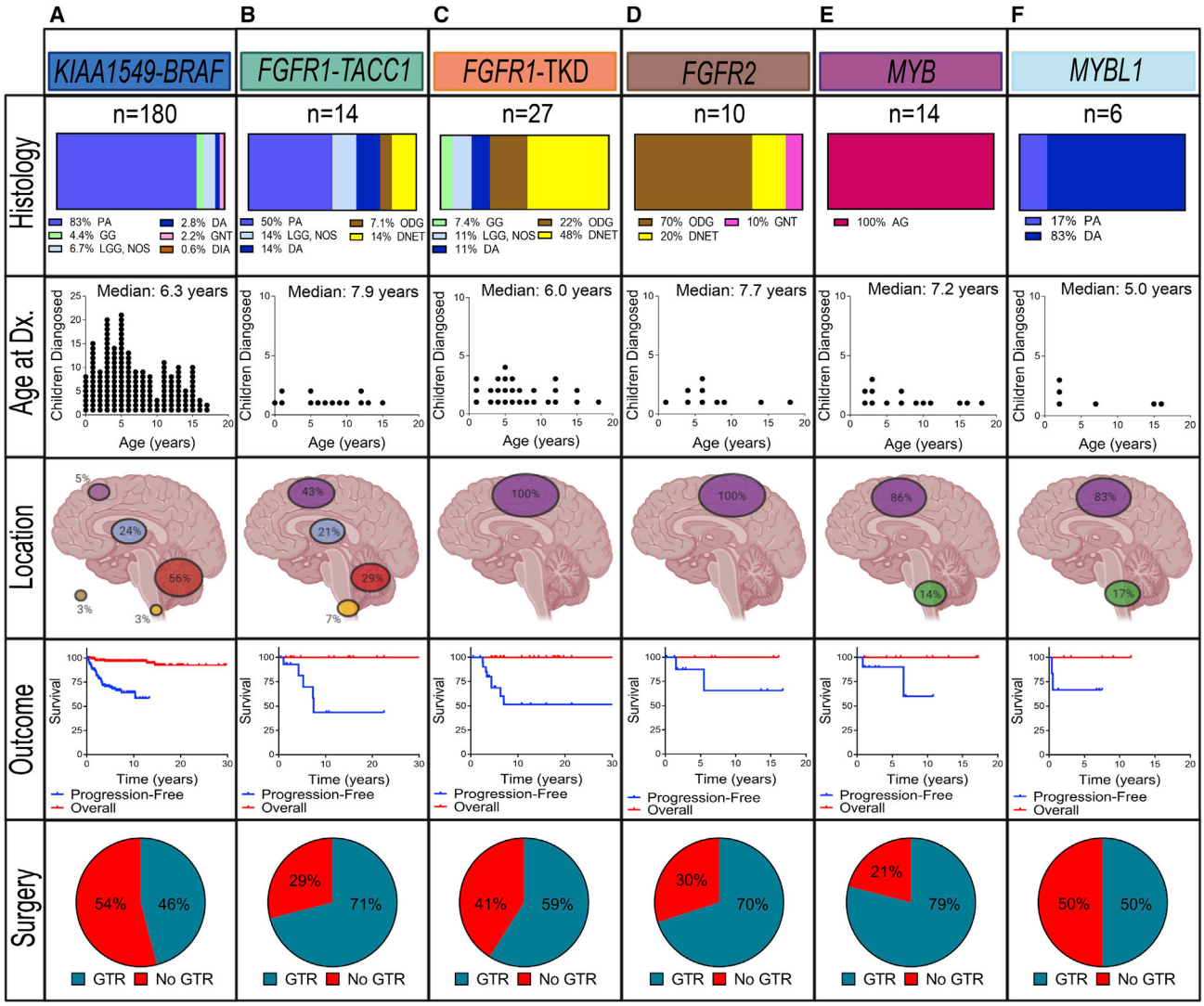

Figure 5. Clinicopathologic Features of Rearrangement-Driven pLGG

Schematic representation of key clinical features and outcomes for (A) *KIAA1549-BRAF*, (B) *FGFR1-TACC1*, (C) FGFR1 TKD, (D) *FGFR2* fusions, (E) *MYB*, and (F) *MYBL1*. PA, pilocytic astrocytoma; LGG, NOS, low-grade glioma, not otherwise specified; GG, ganglioglioma; DNET, dysembryoplastic neuroepithelial tumor; PXA, pleomorphic xanthoastrocytoma; GNT, glioneuronal tumor; DA, diffuse astrocytoma; AG, angiocentric glioma; ODG, oligodendroglioma; DIA/DIG, desmoplastic infantile astrocytoma/ganglioglioma; Dx, diagnosis; GTR, gross total resection. See also Figures S4 and S5 and Table S4.

of 55%) BRAF p.V600E tumors had inferior PFS to *KIAA1549-BRAF* (5-year PFS of 69%) fused tumors (p = 0.0139 and p = 0.0356, respectively, log rank test, Figures S7A and S7B), despite their OS not being significantly different (p = 0.1169 and 0.1888, respectively, log rank test, Figures S7C and S7D).

FGFR1 Mutations

FGFR1 point mutations were observed in 1.5% of pLGG and primarily consisted of p.N546K and p.K656E. Histologically, these tumors were most frequently dysembryoplastic neuroepithelial tumors (n = 13, 41%) or pilocytic astrocytoma (n = 9, 28%), diagnosed in older children (p = 0.032, Fisher's exact test), and often (n = 16, 50%) co-occurred with multiple genetic alterations, including NF1 (n = 7, 22%) or additional RAS/MAPK pathway mutations (n = 11, 34%) (Figures 2A and 6B). Interestingly, in some cases, multiple point mutations in *FGFR1* were seen (n = 6, 19%). Of those not lost to follow-up, 43% (n = 12) progressed rapidly (median of 2.2 years, 5-year PFS of 53%). Despite this, only two cases had late deaths after 13.7 and 15.5 years, respectively, both of whom had additional alterations.

IDH1 p.R132H

IDH1 mutations are common in adult lower-grade gliomas, arising in approximately 70% of grade II and III tumors (Parsons et al., 2008; Yan et al., 2009, Balss et al., 2008). In pLGG, IDH1 p.R132H mutations were extremely rare, accounting for only 0.8% of cases (Figure 2B). Most IDH1 p.R132H patients presented with a prolonged history of seizures, sometimes years before the biopsy was performed. All tumors were restricted to the cerebral hemispheres and were either oligodendroglioma or diffuse astrocytoma (Figure 6C). Patients harboring IDH1 p.R132H were diagnosed in late childhood (median: 15.7 years),

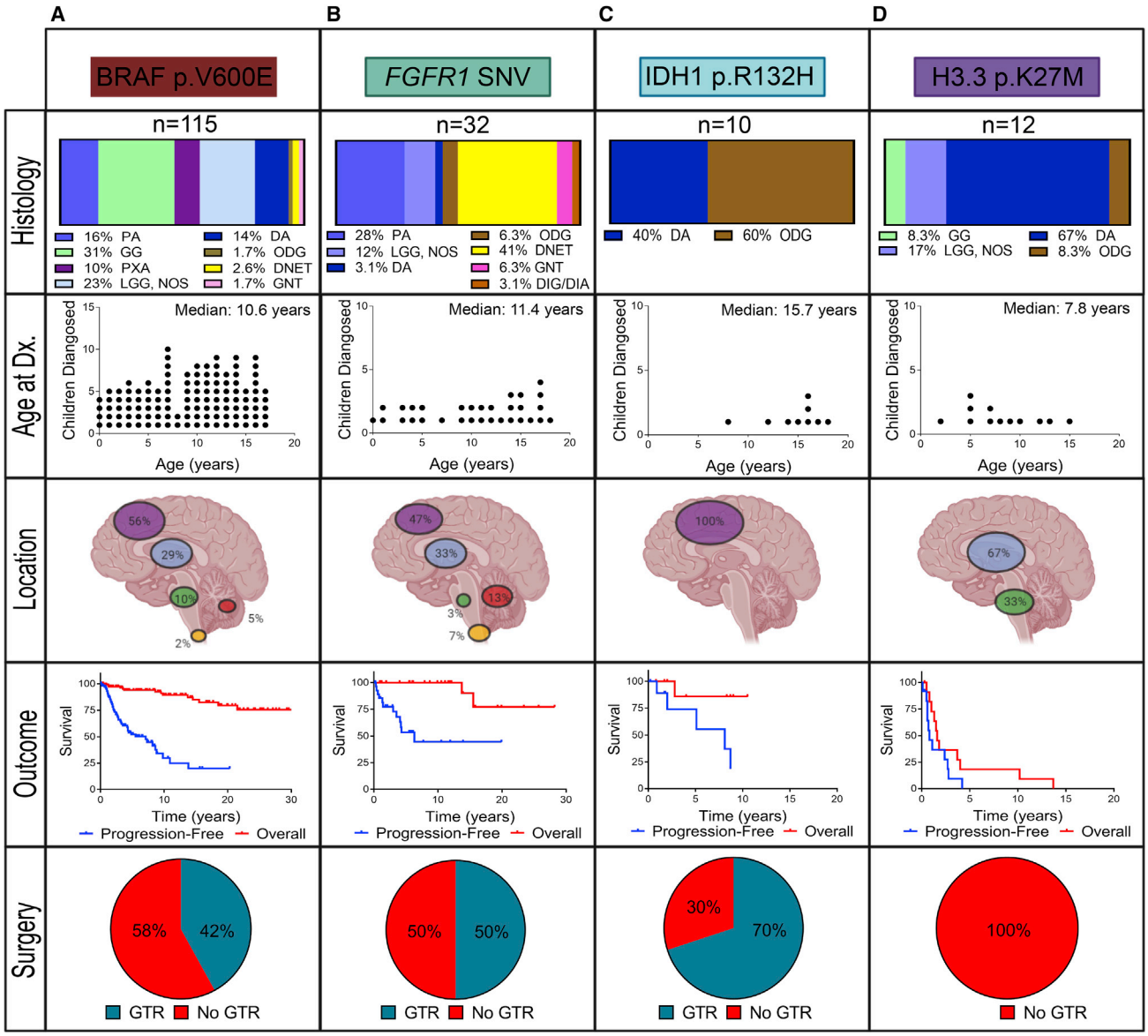

Figure 6. Clinicopathologic Features of SNV-Driven pLGG

Schematic representation of key clinical features and outcomes for (A) BRAF p.V600E, (B) FGFR1 SNVs, (C) IDH1 p.R132H, and (D) H3.3 p.K27M. PA, pilocytic astrocytoma; LGG, NOS, low-grade glioma, not otherwise specified; GG, ganglioglioma; DNET, dysembryoplastic neuroepithelial tumor; PXA, pleomorphic xanthoastrocytoma; GNT, glioneuronal tumor; DA, diffuse astrocytoma; AG, angiocentric glioma; ODG, oligodendroglioma; DIA/DIG, desmoplastic infantile astrocytoma/ganglioglioma; Dx, diagnosis; GTR, gross total resection. See also Figures S6 and S7.

with the youngest patient diagnosed at 8.9 years (Figure 6C). Fifty percent of IDH1 p.R132H pLGG progressed within a median of 5.1 years (5-year PFS of 56%) despite only one succumbing to their disease (Figure 6C).

H3.3 p.K27M

H3F3A mutations are common in childhood high-grade gliomas and DIPG and confer a dismal outcome (Khuong-Quang et al., 2012; Buczkowicz et al., 2014). In our pLGG series, all *H3F3A* mutations were p.K27M, with no p.G34R/V alterations identified (Table S1). These cases were restricted to the midline (diencephalon [n = 8] and brainstem [n = 4]), enriched for diffuse astrocytomas (n = 8, 67%, p = 0.0011, Fisher's exact test), and like other SNVs, often co-occurred with other alterations (25%), most often with BRAF p.V600E (Figures 2A and 6D). Although morphologically and clinically different than midline HGG, H3.3 p.K27M patients progressed early (median time to progression = 0.8 years), with all patients eventually succumbing to their disease (Figure 6D). These data support the role of H3.3 p.K27M as a marker of aggressive behavior regardless of the initial morphology and presentation.

Molecular-Based Risk Stratification for pLGG

Based on the above data, we define a risk stratification for children with pLGG (Figure 7A). pLGG harboring gene fusions or germline

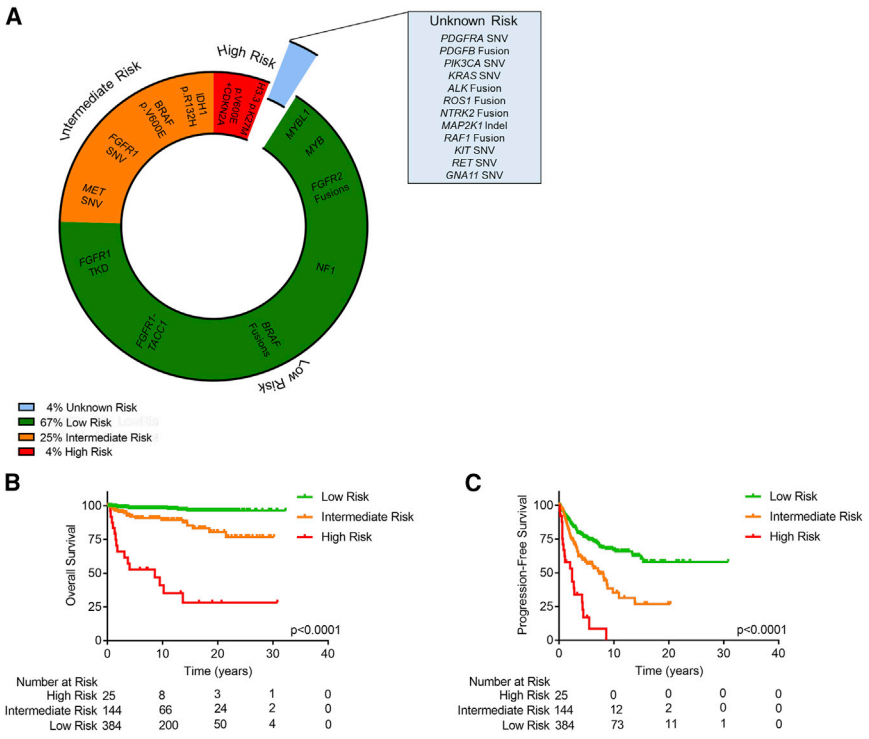

Figure 7. Risk Stratification of pLGG

(A) Donut plot representing assigned risk portfolio of pLGG and their associated biomarkers. Risk assignment is based on the incidence of progression and/or death. In samples harboring multiple alterations, the highest potential risk group was assigned. Alterations appearing in less than five samples are not assigned a risk group.

(B) Kaplan-Meier plot of overall survival of cases separated by risk. p value calculated via the log rank test.

(C) Kaplan-Meier plot of progression-free of cases separated by risk. p value calculated via the log rank test.

See also Figure S8 Table S5.

NF1 mutations comprise the low-risk group. These tumors progress less frequently and often eventually stop growing with very few progressions seen after 10 years and almost no deaths at 20 years follow-up (10-year PFS of 67% and OS of 98%, 20-year PFS and OS of 58% and 96%, respectively) (Figures 7B and 7C). These tumors require conservative management as therapy may carry higher long-term morbidity than the tumor itself.

The intermediate-risk group of pLGG includes tumors with BRAF p.V600E without *CDKN2A* deletion, *FGFR1* SNV, IDH1 p.R132H, or *MET* mutations. Intermediate-risk tumors had a 10-year PFS and OS of 35% and 90%, respectively (Figures 7B and 7C). However, in contrast to the low-risk tumors, these tumors continue to progress with a 20-year PFS of 27% and 20-year OS of 81%. Furthermore, they have a propensity for acquiring additional alterations, which may result in the need to refine treatment over time. These patients may therefore require multiple treatment courses and longer-term follow-up than the low-risk patients due to the risk of late death.

High-risk pLGG include those with H3.3 p.K27M, or BRAF p.V600E with *CDKN2A* deletion. These tumors invariably progress (10-year PFS of 0%) and these patients often succumb to their disease (10-year OS of 41%) (Figures 7B and 7C). Patients with H3.3 p.K27M do worse than those with BRAF p.V600E and *CDKN2A* deletion (10-year PFS and OS of 0% and 35% and 0% and 60%, respectively), but both do far worse than low- and intermediate-risk patients. Although H3.3 p.K27M tumors are more likely to result in patient death, both H3.3 p.K27M and BRAF p.V600E and *CDKN2A* deletions result in rapid progression, indicating a need for immediate, aggressive treatment and the introduction of novel, targeted agents.

Finally, pLGG with an undetermined molecular alteration (and hence risk category) showed PFS and OS trends consistent with representation of both low and intermediate risk (10-year PFS and OS of 51% and 92%, respectively, and 20-year PFS and OS of 34% and 89%) (Figures S8A and S8B).

In multivariate analysis, including tumor location (midline), age at diagnosis, sex, extent of resection (GTR), and histological grade, risk group was determined to be the most significant predictor of both progression (hazard ratio = 4.030 [2.030–7.998], $p < 0.0001$, Cox proportional hazards model) and death (hazard ratio = 16.547 [4.556–59.958], $p < 0.0001$, Cox proportional hazards model) (Table S5).

DISCUSSION

Molecular studies of pLGG over the last decade have uncovered oncogenic drivers shown to activate the RAS/MAPK pathway (Collins et al., 2015; Jones et al., 2008; Schindler et al., 2011; Dougherty et al., 2010; Lassaletta et al., 2017; Listernick et al., 1999; Uusitalo et al., 2016; Seminog and Goldacre, 2013). However, despite these advances, the extent of molecular diversity, the frequency of alterations in a population-based setting, and the clinical significance of these diverse alterations are poorly understood. In this study we perform combined morphological, clinical, and molecular profiling of pLGG on a population-based cohort with extensive clinical follow-up. This allowed us to comprehensively investigate the molecular underpinnings and provide comprehensive clinical insights for some of the rarest of pLGG molecular subtypes. Furthermore, we introduce a robust risk stratification system for pLGG, which has the potential to significantly influence the management of these tumors.

RAS/MAPK activation and pLGG were first linked due to the appearance of OPGs in patients with NF1 (Listernick et al., 1999) and this was further supported upon the discovery of *KIAA1549-BRAF* and BRAF p.V600E in these tumors (Jones et al., 2008; Schindler et al., 2011). Here, 378 tumors from 2000 to 2017 had an identifiable alteration affecting the RAS/MAPK pathway with an additional ten showing upregulation via ssGSEA analysis of RNA sequencing data. Therefore, of those we could exhaustively profile (including RNA sequencing), 95% (388/410) showed upregulation of the RAS/MAPK pathway.

Thus, pLGG patients may benefit from RAS/MAPK pathway inhibitors even if no genomic alteration in the pathway is identified. Indeed, this is supported by recent work showing favorable responses to MEK inhibitors in pLGG (Fangusaro et al., 2019). Future work will inevitably look to investigate the alternative mechanisms of RAS/MAPK activation in molecularly silent cases which may include alternative splicing (Siegfried et al., 2013), epigenetic changes, or miRNA alterations (Paroo et al., 2009). However, understanding the specifics of these mechanisms need not hinder the adoption of updated treatment protocols that exploit the RAS/MAPK dependence of these tumors.

Our comprehensive approach to profiling these tumors included morphologic, clinical, and molecular interrogation. In utilizing these approaches, we were able to provide insights into the clinical features of the rarest molecular entities of pLGG (Figures 5B–5F and 6B–6D) and provide disease stratification based on the type of molecular alteration driving the tumor (Figures 4C, 4D, 7B, and 7C). In our dataset, rearrangement-driven pLGG had a younger age of onset, were enriched for WHO grade I histology, and had a less-aggressive clinical course (Figures 4B–4D). This suggests that these oncogenic alterations may occur early in development, promoting tumor initiation in a developmental context permissive for one-hit tumorigenesis. Previous work identified that *BRAF* fusions promoted gliogenesis in region-specific neural stem cell populations, while having little effect in differentiated astrocytes (Kaul et al., 2012). When originally identified, *KIAA1549-BRAF* was shown to have higher kinase activity than BRAF p.V600E (Jones et al., 2008). This may help explain why many *KIAA1549-BRAF* pLGG undergo spontaneous growth arrest; an environment where too much RAS/MAPK upregulation promotes senescence and too little fails to initiate tumor growth (Jacob et al., 2011; Raabe et al., 2011). In comparison, SNV-driven pLGG were more commonly diagnosed at a later age, consistent with these alterations being acquired later in development. Furthermore, SNV-driven pLGG co-occurred with additional SNVs, but never co-harbored fusion events; displaying a pattern of mutual exclusivity as seen across many cancer types (Gao et al., 2018). Finally, SNV-driven pLGG were associated with poorer outcome. Future work will need to compare the mechanisms behind rearrangements and SNVs in pLGG to elucidate why the observed clinical differences occur.

These results enabled us to develop a risk-based stratification system for pLGG (Figure 7A). Genetic rearrangements, including all fusions and duplications, as well as germline *NF1* inactivation, are considered low risk. As these tumors are rarely fatal, we propose they should be managed expectantly, with careful consideration of additional treatment after surgery, and radiation excluded from all post-operative treatment. For example, for asymptomatic NF1-driven pLGG, surveillance is justified. However, if patients display progressive symptoms, most often as vision loss, treatment with chemotherapy (Mahoney et al., 2000; Packer et al., 1997) or targeted inhibitors (Banerjee et al., 2017; Fangusaro et al., 2019) can be beneficial. Beyond 10 years these tumors are much less likely to recur and the frequency of follow-up may potentially be reduced. Intermediate-risk pLGG are SNV-driven tumors, including those with *BRAF* or *FGFR1* SNVs. These frequently harbor more than one alteration and have a higher risk of recurrence which extends beyond 10 years. These patients may require multiple treatments and longer follow-up than low-risk patients. Importantly, compared with high-risk patients, intermediate-risk tumors rarely die of their disease, so efforts should focus on mitigating clinical progression. Finally, high-risk tumors harboring H3.3 p.K27M or BRAF p.V600E and *CDKN2A* deletion may require new approaches to improve survival, including the development of novel agents as well as combination therapies to promote synthetic lethality. Importantly, as the era of novel targeted therapies such as BRAF and MEK inhibitors inevitably arrives, the risk stratifications of these high- and intermediate-risk pLGG may change. Nevertheless, significant long-term follow-up is required to determine if the above is indeed true. The large number of patients in this cohort, long-term clinical follow-up data, and the similarity between subgroups suggest that these findings are robust and provide reliable information of critical importance to clinicians today.

In conclusion, this comprehensive molecular landscape of the clinical and molecular features of pLGG provides clinicians with an invaluable resource for the management of common and rare molecular pLGG subtypes. These data can guide diagnostic protocols and treatment approaches while aiding in expediting clinical trials for new, better-targeted therapies for these children in the near future.

STAR★METHODS

Detailed methods are provided in the online version of this paper and include the following:

- KEY RESOURCES TABLE
- LEAD CONTACT AND MATERIALS AVAILABILITY
- EXPERIMENTAL MODEL AND SUBJECT DETAILS
  - Patient Samples
- METHOD DETAILS
  - Nucleic Acid Extraction
  - Droplet Digital PCR
  - NanoString nCounter Analysis
  - NanoString nCounter Vantage 3D for Protein Analysis
  - Fluorescent In Situ Hybridization
  - Immunohistochemistry
  - SNP Array
  - Targeted DNA Sequencing
  - Whole Transcriptome Sequencing
  - Gene Set Enrichment Analysis
  - Genetic Analysis at Collaborating Institutions
- QUANTIFICATION AND STATISTICAL ANALYSIS
- DATA AND CODE AVAILABILITY

SUPPLEMENTAL INFORMATION

Supplemental Information can be found online at https://doi.org/10.1016/j.ccell.2020.03.011.

ACKNOWLEDGMENTS

This work was supported by endowed funds from the Government of Canada through Genome Canada and the Ontario Genomics Institute (OGI-121); A Kid's Brain Tumor Cure; Brain Tumor Research Assistance and Information Network; The Pediatric Low-Grade Astrocytoma Foundation; Meagan's Walk; B.r.a.i.n.child Canada; Canadian Cancer Society (grant no. 702296); Canadian Institutes of Health Research (grant no. 159805); Restracomp

Scholarship and Fellowship funds from the Garron Family Chair in Childhood Cancer Research at The Hospital for Sick Children (to S.R., M.Z., A.L., and K.F.); Canadian Institutes of Health Research (CGS-M) scholarship (to S.R.); Ontario Graduate Scholarship (to S.R.); Tokyo Children's Cancer Study Group (TCCSG) scholarship of the Gold Ribbons Network of Japan (to K.F.); The Marie-Josée and Henry R. Kravis Center for Molecular Oncology; The National Cancer Institute Cancer Center Core grant no. P30-CA008748; The American Lebanese Syrian Associated Charities (ALSAC) of St. Jude Children's Research Hospital.

We thank colleagues Sergio Pereira and Jo-Anne Herbrick (both at the Center for Applied Genomics at SickKids, Toronto, ON, Canada) for facilitating our work in addition to Paula Marrano, Famida Spatare, and Monte Borden (Department of Pathology, the Hospital for Sick Children, Toronto) and Cindy Zhang (Brain Tumor Research Center, The Hospital for Sick Children, Toronto). We further acknowledge the Members of the Molecular Diagnostics Service in the Department of Pathology (MSK, New York, USA).

AUTHOR CONTRIBUTIONS

S.R., M.Z., U.T., and C.H. conceived the project and led the study. Molecular characterization of samples from HSC were completed by S.R., M.Z., K.F., L.N., A.G.-S., J.B., A.L., M.J., and J.S. under the supervision of A.A., P.E.K., S.J., M.S., U.T., and C.H. Molecular characterization of samples from partnering institutions were completed by R.G.T., W.O., I.Q., L.F.S., M.I.L., A.J.W., S.G., M.R., T.B., D.S.T., N.L., and C.D'A. under supervision from M.A.K., M. Santi., and D.W.E. R.G.T., W.O., I.Q., L.F.S., M.I.L., A.J.W., S.G., M.R., T.B., D.S.T., N.L., C.D'A., A.K., G.M.I., J.D., P.D., M.D.T., J.T.R., S.L., M. Shroff., M. Shago., L.-N.H., V.R., E.B., U.B., A.H., M.A.K., M. Santi., and D.W.E. provided patient-related materials and/or clinical data used in this study. Histopathological analysis was completed by A.A., M. Shago., C.D'A., and C.H. Array and NGS data were processed and analyzed by S.R., R.S., and C.L. under supervision from U.T. and C.H. Statistical analysis was done by S.R., M.Z., R.S., and C.L. U.T. and C.H provided overall supervision for the project and wrote the manuscript with S.R. and M.Z. and with input from M.A.K., M. Santi., and D.W.E. All authors reviewed the manuscript and figures before submission.

DECLARATION OF INTERESTS

The authors declare no competing interests.

Received: January 3, 2020
Revised: January 27, 2020
Accepted: March 12, 2020
Published: April 13, 2020

REFERENCES

Aghajan, Y., Levy, M.L., Malicki, D.M., and Crawford, J.R. (2016). Novel PPP1CB-ALK fusion protein in a high-grade glioma of infancy. BMJ Case Rep. *16*, 2016.

Anders, S., Pyl, P.T., and Huber, W. (2015). HTSeq-A Python framework to work with high-throughput sequencing data. Bioinformatics *31*, 166–169.

Balss, J., Meyer, J., Mueller, W., Korshunov, A., Hartmann, C., and von Deimling, A. (2008). Analysis of the IDH1 codon 132 mutation in brain tumors. Acta Neuropathol. *116*, 597–602.

Bandopadhayay, P., Ramkissoon, L.A., Jain, P., Bergthold, G., Wala, J., Zeid, R., Schumacher, S.E., Urbanski, L., O'Rourke, R., Gibson, W.J., et al. (2016). MYB-QKI rearrangements in angiocentric glioma drive tumorigenicity through a tripartite mechanism. Nat. Genet. *48*, 273–282.

Banerjee, A., Jakacki, R.I., Onar-Thomas, A., Wu, S., Nicolaides, T., Young Poussaint, T., Fangusaro, J., Phillips, J., Perry, A., Turner, D., et al. (2017). A phase I trial of the MEK inhibitor selumetinib (AZD6244) in pediatric patients with recurrent or refractory low-grade glioma: a Pediatric Brain Tumor Consortium (PBTC) study. Neuro Oncol. *19*, 1135–1144.

Benelli, M., Pescucci, C., Marseglia, G., Severgnini, M., Torricelli, F., and Magi, A. (2012). Discovering chimeric transcripts in paired-end RNA-seq data by using EricScript. Bioinformatics *28*, 3232–3239.

Broniscer, A., Baker, S.J., West, A.N., Fraser, M.M., Proko, E., Kocak, M., Dalton, J., Zambetti, G.P., Ellison, D.W., Kun, L.E., et al. (2007). Clinical and molecular characteristics of malignant transformation of low-grade glioma in children. J. Clin. Oncol. *25*, 682–689.

Buczkowicz, P., Bartels, U., Bouffet, E., Becher, O., and Hawkins, C. (2014). Histopathological spectrum of paediatric diffuse intrinsic pontine glioma: diagnostic and therapeutic implications. Acta Neuropathol. *128*, 573–581.

Cheng, D.T., Mitchell, T.N., Zehir, A., Shah, R.H., Benayed, R., Syed, A., Chandramohan, R., Liu, Z.Y., Won, H.H., Scott, S.N., et al. (2015). Memorial Sloan Kettering-integrated mutation profiling of actionable cancer targets (MSK-IMPACT): a hybridization capture-based next-generation sequencing clinical assay for solid tumor molecular oncology. J. Mol. Diagn. *17*, 251–264.

Collins, V.P., Jones, D.T., and Giannini, C. (2015). Pilocytic astrocytoma: pathology, molecular mechanisms and markers. Acta Neuropathol. *129*, 775–788.

D'Angelo, F., Ceccarelli, M., Tala, Garofano, L., Zhang, J., Frattini, V., Caruso, F.P., Lewis, G., Alfaro, K.D., Bauchet, L., et al. (2019). The molecular landscape of glioma in patients with neurofibromatosis 1. Nat. Med. *25*, 176–187.

Dobin, A., Davis, C.A., Schlesinger, F., Drenkow, J., Zaleski, C., Jha, S., Batut, P., Chaisson, M., and Gingeras, T.R. (2013). STAR: ultrafast universal RNA-seq aligner. Bioinformatics *29*, 15–21.

Dougherty, M.J., Santi, M., Brose, M.S., Ma, C., Resnick, A.C., Sievert, A.J., Storm, P.B., and Biegel, J.A. (2010). Activating mutations in BRAF characterize a spectrum of pediatric low-grade gliomas. Neuro Oncol. *12*, 621–630.

Fangusaro, J., Onar-Thomas, A., Young Poussaint, T., Wu, S., Ligon, A.H., Lindeman, N., Banerjee, A., Packer, R.J., Kilburn, L.B., Goldman, S., et al. (2019). Selumetinib in paediatric patients with BRAF-aberrant or neurofibromatosis type 1-associated recurrent, refractory, or progressive low-grade glioma: a multicentre, phase 2 trial. Lancet Oncol. *20*, 1011–1022.

Fina, F., Barets, D., Colin, C., Bouvier, C., Padovani, L., Nanni-Metellus, I., Ouafik, L., Scavarda, D., Korshunov, A., Jones, D.T., et al. (2017). Droplet digital PCR is a powerful technique to demonstrate frequent FGFR1 duplication in dysembryoplastic neuroepithelial tumors. Oncotarget *8*, 2104–2113.

Gao, Q., Liang, W.W., Foltz, S.M., Mutharasu, G., Jayasinghe, R.G., Cao, S., Liao, W.W., Reynolds, S.M., Wyczalkowski, M.A., Yao, L., et al. (2018). Driver fusions and their implications in the development and treatment of human cancers. Cell Rep. *23*, 227–238.

Ge, H., Liu, K., Juan, T., Fang, F., Newman, M., and Hoeck, W. (2011). FusionMap: detecting fusion genes from next-generation sequencing data at base-pair resolution. Bioinformatics *27*, 1922–1928.

Greenberg, M.L., Barr, R.D., DiMonte, B., McLaughlin, E., and Greenberg, C. (2003). Childhood cancer registries in Ontario, Canada: lessons learned from a comparison of two registries. Int. J. Cancer *105*, 88–91.

Guerreiro Stucklin, A.S., Ryall, S., Fukuoka, K., Zapotocky, M., Lassaletta, A., Li, C., Bridge, T., Kim, B.S., Arnoldo, A., Kowalski, P.E., et al. (2019). Alterations in ALK/ROS1/NTRK/MET drive a group of infantile hemispheric gliomas. Nat. Commun. *10*, 4343.

Gutmann, D.H., Ferner, R.E., Listernick, R.H., Korf, B.R., Wolters, P.L., and Johnson, K.J. (2017). Neurofibromatosis type 1. Nat. Rev. Dis. Primers *3*, 17004.

Hartmann, C., Meyer, J., Balss, J., Capper, D., Mueller, W., Christians, A., Felsberg, J., Wolter, M., Mawrin, C., Wick, W., et al. (2009). Type and frequency of IDH1 and IDH2 mutations are related to astrocytic and oligodendroglial differentiation and age: a study of 1,010 diffuse gliomas. Acta Neuropathol. *118*, 469–474.

Jacob, K., Quang-Khuong, D.A., Jones, D.T., Witt, H., Lambert, S., Albrecht, S., Witt, O., Vezina, C., Shirinian, M., Faury, D., et al. (2011). Genetic aberrations leading to MAPK pathway activation mediate oncogene-induced senescence in sporadic pilocytic astrocytomas. Clin. Cancer Res. *17*, 4650–4660.

Jones, D.T., Kocialkowski, S., Liu, L., Pearson, D.M., Bäcklund, L.M., Ichimura, K., and Collins, V.P. (2008). Tandem duplication producing a novel

oncogenic BRAF fusion gene defines the majority of pilocytic astrocytomas. Cancer Res. *68*, 8673–8677.

Jones, D.T., Gronych, J., Lichter, P., Witt, O., and Pfister, S.M. (2012). MAPK pathway activation in pilocytic astrocytoma. Cell Mol Life Sci. *69*, 1799–1811.

Jones, D.T., Hutter, B., Jäger, N., Korshunov, A., Kool, M., Warnatz, H.J., Zichner, T., Lambert, S.R., Ryzhova, M., Quang, D.A., et al. (2013). Recurrent somatic alterations of FGFR1 and NTRK2 in pilocytic astrocytoma. Nat. Genet. *45*, 927–932.

Kaul, A., Chen, Y.H., Emnett, R.J., Dahiya, S., and Gutmann, D.H. (2012). Pediatric glioma-associated KIAA1549:BRAF expression regulates neuroglial cell growth in a cell type-specific and mTOR-dependent manner. Genes Dev. *26*, 2561–2566.

Khuong-Quang, D.A., Buczkowicz, P., Rakopoulos, P., Liu, X.Y., Fontebasso, A.M., Bouffet, E., Bartels, U., Albrecht, S., Schwartzentruber, J., Letourneau, L., et al. (2012). K27M mutation in histone H3.3 defines clinically and biologically distinct subgroups of pediatric diffuse intrinsic pontine gliomas. Acta Neuropathol. *124*, 439–447.

Kiehna, E.N., Arnush, M.R., Tamrazi, B., Cotter, J.A., Hawes, D., Robison, N.J., Fong, C.Y., Estrine, D.B., Han, J.H., and Biegel, J.A. (2017). Novel GOPC(FIG)-ROS1 fusion in a pediatric high-grade glioma survivor. J. Neurosurg. Pediatr. *20*, 51–55.

Kim, D., and Salzberg, S.L. (2011). TopHat-Fusion: an algorithm for discovery of novel fusion transcripts. Genome Biol. *12*, R72.

Krishnatry, R., Zhukova, N., Guerreiro Stucklin, A.S., Pole, J.D., Mistry, M., Fried, I., Ramaswamy, V., Bartels, U., Huang, A.8, Laperriere, N., et al. (2016). Clinical and treatment factors determining long-term outcomes for adult survivors of childhood low-grade gliomas. Cancer *122*, 1261–1269.

Lassaletta, A., Zapotocky, M., Mistry, M., Ramaswamy, V., Honnorat, M., Krishnatry, R., Guerreiro Stucklin, A., Zhukova, N., Arnoldo, A., Ryall, S., et al. (2017). Therapeutic and prognostic implications of BRAF V600E in pediatric low-grade gliomas. J. Clin. Oncol. *35*, 2934–2941.

Li, B., and Dewey, C.N. (2011). RSEM: accurate transcript quantification from RNA-seq data with or without a reference genome. BMC Bioinformatics *12*, 323.

Listernick, R., Charrow, J., and Gutmann, D.H. (1999). Intracranial gliomas in neurofibromatosis type 1. Am. J. Med. Genet. *89*, 38–44.

Louis, D.N., Perry, A., Reifenberger, G., von Deimling, A., Figarella-Branger, D., Cavenee, W.K., Ohgaki, H., Wiestler, O.D., Kleihues, P., and Ellison, D.W. (2016). The 2016 World Health Organization classification of tumors of the central nervous system: a summary. Acta Neuropathol. *131*, 803–820.

Mahoney, D.H., Jr., Cohen, M.E., Friedman, H.S., Kepner, J.L., Gemer, L., Langston, J.W., James, H.E., Duffner, P.K., and Kun, L.E. (2000). Carboplatin is effective therapy for young children with progressive optic pathway tumors: a Pediatric Oncology Group phase II study. Neuro Oncol. *2*, 213–220.

McPherson, A., Hormozdiari, F., Zayed, A., Giuliany, R., Ha, G., Sun, M.G., Griffith, M., Heravi Moussavi, A., Senz, J., Melnyk, N., et al. (2011). deFuse: an algorithm for gene fusion discovery in tumor RNA-seq data. PLoS Comput. Biol. *7*, e1001138.

Mistry, M., Zhukova, N., Merico, D., Rakopoulos, P., Krishnatry, R., Shago, M., Stavropoulos, J., Alon, N., Pole, J.D., Ray, P.N., et al. (2015). BRAF mutation and CDKN2A deletion define a clinically distinct subgroup of childhood secondary high-grade glioma. J. Clin. Oncol. *33*, 1015–1022.

Nageswara Rao, A.A., and Packer, R.J. (2014). Advances in the management of low-grade gliomas. Curr. Oncol. Rep. *16*, 398.

Northcott, P.A., Pfister, S.M., and Jones, D.T. (2015). Next-generation (epi)genetic drivers of childhood brain tumors and the outlook for targeted therapies. Lancet Oncol. *16*, e293–e302.

Ostrom, Q.T., de Blank, P.M., Kruchko, C., Petersen, C.M., Liao, P., Finlay, J.L., Stearns, D.S., Wolff, J.E., Wolinsky, Y., Letterio, J.J., and Barnholtz-Sloan, J.S. (2015). Alex's Lemonade Stand Foundation infant and childhood primary brain and central nervous system tumors diagnosed in the United States in 2007–2011. Neuro Oncol. *16* (*Suppl 10*), x1–x36.

Packer, R.J., Ater, J., Allen, J., Phillips, P., Geyer, R., Nicholson, H.S., Jakacki, R., Kurczynski, E., Needle, M., Finlay, J., et al. (1997). Carboplatin and vincristine chemotherapy for children with newly diagnosed progressive low-grade gliomas. J. Neurosurg. *86*, 747–754.

Paroo, Z., Ye, X., Chen, S., and Liu, Q. (2009). Phosphorylation of the human microRNA-generating complex mediates MAPK/Erk signaling. Cell *139*, 112–122.

Parsons, D.W., Jones, S., Zhang, X., Lin, J.C., Leary, R.J., Angenendt, P., Mankoo, P., Carter, H., Siu, I.M., Gallia, G.L., et al. (2008). An integrated genomic analysis of human glioblastoma multiforme. Science *321*, 1807–1812.

Qaddoumi, I., Orisme, W., Wen, J., Santiago, T., Gupta, K., Dalton, J.D., Tang, B., Haupfear, K., Punchihewa, C., Easton, J., et al. (2016). Genetic alterations in uncommon low-grade neuroepithelial tumors: BRAF, FGFR1, and MYB mutations occur at high frequency and align with morphology. Acta Neuropathol. *131*, 833–845.

Raabe, E.H., Lim, K.S., Kim, J.M., Meeker, A., Mao, X.G., Nikkhah, G., Maciaczyk, J., Kahlert, U., Jain, D., Bar, E., et al. (2011). BRAF activation induces transformation and then senescence in human neural stem cells: a pilocytic astrocytoma model. Clin. Cancer Res. *17*, 3590–3599.

Ramkissoon, L.A., Horowitz, P.M., Craig, J.M., Ramkissoon, S.H., Rich, B.E., Schumacher, S.E., McKenna, A., Lawrence, M.S., Bergthold, G., Brastianos, P.K., et al. (2013). Genomic analysis of diffuse pediatric low-grade gliomas identifies recurrent oncogenic truncating rearrangements in the transcription factor MYBL1. Proc. Natl. Acad. Sci. U S A *110*, 8188–8193.

Robinson, M.D., McCarthy, D.J., and Smyth, G.K. (2010). edgeR: a Bioconductor package for differential expression analysis of digital gene expression data. Bioinformatics *26*, 139–140.

Rusch, M., Nakitandwe, J., Shurtleff, S., Newman, S., Zhang, Z., Edmonson, M.N., Parker, M., Jiao, Y., Ma, X., Liu, Y., et al. (2018). Clinical cancer genomic profiling by three-platform sequencing of whole genome, whole exome and transcriptome. Nat. Commun. *9*, 3962.

Ryall, S., Krishnatry, R., Arnoldo, A., Buczkowicz, P., Mistry, M., Siddaway, R., Ling, C., Pajovic, S., Yu, M., Rubin, J.B., et al. (2016). Targeted detection of genetic alterations reveal the prognostic impact of H3K27M and MAPK pathway aberrations in paediatric thalamic glioma. Acta Neuropathol. Commun. *4*, 93.

Ryall, S., Arnoldo, A., Krishnatry, R., Mistry, M., Khor, K., Sheth, J., Ling, C., Leung, S., Zapotocky, M., Guerreiro Stucklin, A., et al. (2017). Multiplex detection of pediatric low-grade glioma signature fusion transcripts and duplications using the NanoString nCounter system. J. Neuropathol. Exp. Neurol. *76*, 562–570.

Schindler, G., Capper, D., Meyer, J., Janzarik, W., Omran, H., Herold-Mende, C., Schmieder, K., Wesseling, P., Mawrin, C., Hasselblatt, M., et al. (2011). Analysis of BRAF V600E mutation in 1,320 nervous system tumors reveals high mutation frequencies in pleomorphic xanthoastrocytoma, ganglioglioma and extra-cerebellar pilocytic astrocytoma. Acta Neuropathol. *121*, 397–405.

Seminog, O.O., and Goldacre, M.J. (2013). Risk of benign tumours of nervous system, and of malignant neoplasms, in people with neurofibromatosis: population-based record-linkage study. Br. J. Cancer *108*, 193–198.

Siegfried, Z.1, Bonomi, S., Ghigna, C., and Karni, R. (2013). Regulation of the Ras-MAPK and PI3K-mTOR signalling pathways by alternative splicing in cancer. Int. J. Cell Biol. *2013*, 568931.

Subramanian, A., Tamayo, P., Mootha, V.K., Mukherjee, S., Ebert, B.L., Gillette, M.A., Paulovich, A., Pomeroy, S.L., Golub, T.R., Lander, E.S., et al. (2005). Gene set enrichment analysis: a knowledge-based approach for interpreting genome-wide expression profiles. Proc. Natl. Acad. Sci. U S A *102*, 15545–15550.

Surrey, L.F., MacFarland, S.P., Chang, F., Cao, K., Rathi, K.S., Akgumus, G.T., Gallo, D., Lin, F., Gleason, A., Raman, P., et al. (2019). Clinical utility of custom-designed NGS panel testing in pediatric tumors. Genome Med. *11*, 32.

Tatevossian, R.G., Tang, B., Dalton, J., Forshew, T., Lawson, A.R., Ma, J., Neale, G., Shurtleff, S.A., Bailey, S., Gajjar, A., et al. (2010). MYB upregulation and genetic aberrations in a subset of pediatric low-grade gliomas. Acta Neuropathol. *120*, 731–743.

Uusitalo, E., Rantanen, M., Kallionpää, R.A., Pöyhönen, M., Leppävirta, J., Ylä-Outinen, H., Riccardi, V.M., Pukkala, E., Pitkäniemi, J., Peltonen, S., et al. (2016). Distinctive cancer associations in patients with neurofibromatosis type 1. J. Clin. Oncol. *34*, 1978–1986.

Wang, K., Li, M., and Hakonarson, H. (2010). ANNOVAR: functional annotation of genetic variants from high-throughput sequencing data. Nucleic Acids Res. *38*, e164.

Wisoff, J.H., Sanford, R.A., Heier, L.A., Sposto, R., Burger, P.C., Yates, A.J., Holmes, E.J., and Kun, L.E. (2011). Primary neurosurgery for pediatric low-grade gliomas: a prospective multi-institutional study from the Children's Oncology Group. Neurosurgery *68*, 1548–1554.

Wu, G., Diaz, A.K., Paugh, B.S., Rankin, S.L., Ju, B., Li, Y., Zhu, X., Qu, C., Chen, X., Zhang, J., et al. (2014). The genomic landscape of diffuse intrinsic pontine glioma and pediatric non-brainstem high-grade glioma. Nat. Genet. *46*, 444–450.

Yan, H., Parsons, D.W., Jin, G., McLendon, R., Rasheed, B.A., Yuan, W., Kos, I., Batinic-Haberle, I., Jones, S., Riggins, G.J., et al. (2009). IDH1 and IDH2 mutations in gliomas. N. Engl. J. Med. *360*, 765–773.

Zhang, J., Wu, G., Miller, C.P., Tatevossian, R.G., Dalton, J.D., Tang, B., Orisme, W., Punchihewa, C., Parker, M., Qaddoumi, I., et al. (2013). Whole-genome sequencing identifies genetic alterations in pediatric low-grade gliomas. Nat. Genet. *45*, 602–612.

STAR★METHODS

KEY RESOURCES TABLE

REAGENT or RESOURCE	SOURCE	IDENTIFIER
Antibodies		
Mouse Anti-Human BRAF p.V600E Monoclonal Antibody	Spring Bioscience	E19290
Rabbit Anti-Histone H3F3A p.K27M Polyclonal Antibody	Millipore	ABE419
Biological Samples		
Brain tissue tumor specimen	Hospital for Sick Children (Toronto, ON, CAN); St. Jude Children's Hospital (Memphis, TN, USA); Children's Hospital of Philadelphia (Philadelphia, PA, USA); Memorial Sloan Kettering Cancer Center (New York, NY, USA)	NA
Critical Commercial Assays		
QIAamp DNA FFPE Tissue Kit	Qiagen	56404
RNeasy FFPE Kit	Qiagen	73504
DNeasy Blood and Tissue Kit	Qiagen	69504
RNeasy Mini Kit	Qiagen	74104
dsDNA Broad Range Assay Kit	Thermo Fisher	Q32850
RNA Broad Range Assay Kit	Thermo Fisher	Q10210
ddPCR Supermix for probes (no dUTP)	Bio-Rad	1863024
Droplet Generation Oil for Probes	Bio-Rad	1863005
nCounter Elements TagSet	NanoString Technologies	Dependent on panel - contact NanoString
nCounter Preparation Station	NanoString Technologies	NA
BRAF FISH probes	The Center for Applied Genomics (HSC, Toronto, Canada)	NA
MYB FISH probes	The Center for Applied Genomics (HSC, Toronto, Canada)	NA
MYBL1 FISH probes	The Center for Applied Genomics (HSC, Toronto, Canada)	NA
FGFR2 FISH probes	The Center for Applied Genomics (HSC, Toronto, Canada)	NA
Genome-Wide Human SNP Array 6.0	Thermo Fisher	901150
Ampliseq Comprehensive DNA Focus Panel Kit	Illumina	20019164
Ampliseq Library PLUS	Illumina	20019101
Ampliseq CD Indexes	Illumina	20019105
MiSeq Reagent Micro Kit V2	Illumina	MS-103-1002
TruSeq RNA Library Prep Kit v2	Illumina	RS-122-2001/2
Deposited Data		
Ampliseq Targeted DNA Sequencing	This paper	EGAS00001004242
RNA Sequencing	This paper	EGAS00001004242
Oligonucleotides		
N546K FP: 5'- TGATGAAGATGATCGGGAAGC-3'	Fina et al., 2017	N/A
N546K RP: 5'-CACCCACCATCCTGCGT-3'	Fina et al., 2017	N/A
N546K wild-type Probe: AATATCATCAACCTGCTGG	Fina et al., 2017	N/A
N546K Probe: AATATCATCAAACTGCTGG	Fina et al., 2017	N/A

(*Continued on next page*)

Continued

REAGENT or RESOURCE	SOURCE	IDENTIFIER
K656E FP: 5'-CACGGGACATTCACCACATC-3'	Fina et al., 2017	N/A
K656E RP: 5'-CACAGGGCGGCCTTGTC-3'	Fina et al., 2017	N/A
K656E wild-type Probe: CTACTATAAAAAGA CAACCAA	Fina et al., 2017	N/A
K656E Probe: TACTATAAAGAGACAACCAA	Fina et al., 2017	N/A
Software and Algorithms		
Partek	Genomics Suite	https://www.partek.com/partek-genomics-suite/
GISTIC	Broad Institute	software.broadinstitute.org/software/cprg/?q=node/31
BaseSpace	Illumina	https://www.illumina.com/products/by-type/informatics-products/basespace-sequence-hub.html
Isaac Variant Caller	Illumina	https://www.illumina.com/products/by-type/informatics-products/basespace-sequence-hub.html
STAR	Dobin et al., 2013	https://code.google.com/archive/p/rna-star/
TopHat	Johns Hopkins University	ccb.jhu.edu/software/tophat/index.shtml
DeFuse	BC Cancer Agency	http://compbio.bccrc.ca
EricScript	Careggi University Hospital	http://ericscript.sourceforge.net
FusionMap	Amgen Inc	http://www.omicsoft.com/fusionmap
Annovar	Children's Hospital of Philadelphia	annovar.openbioinformatics.org/en/latest/
HTSeq	DKFZ Heidelberg	http://www-huber.embl.de/HTSeq
edgeR	BioConductor	https://bioconductor.org/packages/release/bioc/html/edgeR.html
Gene set enrichment analysis	Broad Institute	http://software.broadinstitute.org/gsea
RSEM	University of Wisconsin-Madison	http://deweylab.biostat.wisc.edu/rsem
GraphPad Prism version 7.00 for Windows	GraphPad Software	https://www.graphpad.com/scientific-software/prism/
IBM SPSS Statistics for Windows	IBM Corp.	https://www.ibm.com/analytics/spss-statistics-software
R	The Comprehensive R Archive Network	r-project.org
Other		
PrimePCR ddPCR mutation assay BRAF wild-type/p.V600E for p.V600E	Bio-Rad	dHsaCP2000027 dHsaCP2000028
PrimePCR ddPCR mutation assay H3F3A wild-type/K28M for p.K28M	Bio-Rad	dHsaCP2500510 dHsaCP2500511
PrimePCR ddPCR mutation assay H3F3A wild-type/G35R for p.G35R	Bio-Rad	dHsaMDS720957813
PCR ddPCR copy number assay CDKN2A	Bio-Rad	dHsaCP1000581
PCR ddPCR copy number assay APB31 (control for CDKN2A)	Bio-Rad	dHsaCP2500348
PrimePCR ddPCR mutation assay BRAF wild-type/p.R132H for p.R132H		dHsaCP2000055 dHsaCP2000056

LEAD CONTACT AND MATERIALS AVAILABILITY

Further information and requests for resources and reagents should be directed to and will be fulfilled by the Lead Contact, Cynthia Hawkins (cynthia.hawkins@sickkids.ca). This study did not generate new unique reagents.

EXPERIMENTAL MODEL AND SUBJECT DETAILS

Patient Samples

Tumor specimens and clinical information were collected according to protocols approved by the Research Ethics Board at all participating institutions. All pLGG diagnosed at the Hospital for Sick Children (SickKids) from 1985-2017 are included in this study. SickKids is the only reference center for children in a population of 5 million people and 97.0% of patients remain in the province qualifying this as a population-based study (Krishnatry et al., 2016; Mistry et al., 2015). For patients older than 18 at the time of clinical data collection, information was extracted from the Pediatric Oncology Group of Ontario Network Information System (POGONIS) (Greenberg et al., 2003). Pathology was reviewed by two neuropathologists (CH and CD). A full description of the samples included are provided in Table S1 including patient sex and age at diagnosis.

To determine the clinical implications of rare alterations, additional cases for which a rare molecular alteration was identified at its originating institute (n=61) with accompanying clinicopathologic and outcome data were included from three participating centers: St. Jude Children's Research Hospital, Children's Hospital of Philadelphia, and Memorial Sloan Kettering Cancer Center. A full description of these samples is provided in Table S3 including patient sex and age at diagnosis.

METHOD DETAILS

Nucleic Acid Extraction

DNA/RNA was extracted from 3-5 10 μM thick scrolls obtained from formalin-fixed paraffin embedded (FFPE) tissue. Extractions were completed using the QIAamp DNA FFPE Tissue Kit or RNeasy FFPE Kit (Qiagen, Valencia, CA). If available, fresh frozen tissue rather than FFPE was used to extract DNA and RNA with the DNeasy Blood and Tissue Kit or RNeasy Mini Kit, respectively being used (Qiagen, Valencia, CA). DNA/RNA was quantified with the Qubit Fluorometer V2.0 using the dsDNA or RNA Broad Range Assay Kit (Thermo Scientific, Waltham, MA). All assay kits were used under the manufacturer's guidelines. Material used for tier 3 molecular profiling underwent further quantification/qualification testing with the 2100 Bioanalyzer using RNA 6000 NanoKit (Agilent, Santa Clara, CA) under manufacturer's specifications.

Droplet Digital PCR

Reactions consisted of 1X ddPCR Supermix for probes (no dUTP) (Bio-Rad, Hercules, CA), 900 nM of HPLC-purified forward and reverse primers, 250 nM of target-specific mutant and wild-type probes, and 10–20 ng of genomic DNA in 20 μl of total volume. Each reaction was mixed with 70 μl of Droplet Generation Oil (Bio-Rad, Hercules, CA), partitioned into a minimum of 10,000 droplets on the QX200 droplet generator (Bio-Rad, Hercules, CA), transferred to a 96-well plate and sealed prior to PCR amplification. PCR cycling conditions were as follows unless otherwise specified:

a. 95°C for 10 min
b. 39 cycles of 94°C for 30 s followed by 55°C for 60 s (with a 2°C s-1 ramp rate)
c. 98°C for 10 min
d. Held at 4°C

Fluorescent intensity was measured with the QX200 Droplet Reader (Bio-Rad, Hercules, CA) and data analysis performed with the QuantaSoft droplet reader software (Bio-Rad, Hercules, CA). Positive and negative droplet populations were detected on a two-dimensional graph and variant allele frequency (VAF) calculated based on the total number of fluorescent-positive droplets. All samples were run in duplicate to ensure validity. Samples were considered positive if a minimum 1% VAF was detected in both duplicate runs and a minimum threshold of 50 fluorescent-positive droplets were detected.

1. BRAF p.V600E: BRAF p.V600E detection was completed as previously described (Lassaletta et al., 2017). PrimePCR ddPCR mutation assay BRAF wild-type/p.V600E for p.V600E, Human (unique assay ID: dHsaCP2000027/28) was used (Bio-Rad, Hercules, CA).
2. H3F3A p.K27M: H3F3A p.K27M detection was completed as previously described (Ryall et al., 2016). PrimePCR ddPCR mutation assay H3F3A wild-type/K28M for p.K28M, Human (unique assay ID: dHsaCP2500510/11) was used (Bio-Rad, Hercules, CA).
3. H3F3A p.G34R: H3F3A p.G34R detection was completed as previously described (Ryall et al., 2016). PrimePCR ddPCR mutation assay H3F3A wild-type/G35R for p.G35R, Human (unique assay ID: dHsaMDS720957813) was used (Bio-Rad, Hercules, CA).
4. FGFR1 TKD: FGFR1 TKD detection was completed as previously described (Fina et al., 2017). Custom primer and probe sequences used for this target are previously described (Fina et al., 2017). PCR cycling conditions were as described above. As described, a ratio value of 1.125 for exon 16 relative to exon 8 were called duplicated.
5. *CDKN2A* Deletion: *CDKN2A* deletion detection was completed as previously described (Lassaletta et al., 2017). PCR ddPCR copy number assay *CDKN2A* (unique assay ID: dHsaCP1000581) (Bio-Rad, Hercules, CA) and a reference prime PCR ddPCR copy number assay *APB31* (unique assay ID: dHsaCP2500348) (Bio-Rad, Hercules, CA) were used.

6. IDH1 p.R132H: IDH1 p.R132H detection was completed as described above. PrimePCR ddPCR mutation assay BRAF wild-type/p.R132H for p.R132H, Human (unique assay ID: dHsaCP2000055/56) was used (Bio-Rad, Hercules, CA).
7. FGFR1 p.N546K, p. K656E: FGFR1 p. N546K, p. K656E detection was completed as described above. Custom primer and probe sequences used for this target are as follows:

N546K FP: 5'- TGATGAAGATGATCGGGAAGC-3'
N546K RP: 5'-CACCCACCATCCTGCGT-3'
N546K wild-type Probe: AATATCATCAACCTGCTGG
N546K Probe: AATATCATCAAACTGCTGG
K656E FP: 5'-CACGGGACATTCACCACATC-3'
K656E RP: 5'-CACAGGGCGGCCTTGTC-3'
K656E wild-type Probe: CTACTATAAAAAGACAACCAA
K656E Probe: TACTATAAAGAGACAACCAA

NanoString nCounter Analysis

Probes that targeted *KIAA1549-BRAF* fusion variants were designed in collaboration with NanoString (Seattle, WA) and samples tested as previously described (Ryall et al., 2017). 200-500 ng of RNA was added to the nCounter Elements TagSet and hybridized for 20 h before being loaded on the NanoString nCounter system (Seattle, WA). Samples were processed on the nCounter Preparation Station and the cartridge scanned at 555 fields of view on the nCounter Digital Analyzer. Raw NanoString counts were background adjusted with a Poisson correction based on the negative control spikes included in each run. This was followed by a technical normalization using the 4 housekeeping transcripts included in each run (*ABCF1*, *ALAS1*, *CLTC*, and *HPRT1*). Data is viewed using a box plot and the extreme statistical outlier (3X the interquartile range (IQR)) method was used to detect the presence of an expressed fusion. A second probe set targeting less common fusion variants in pLGG was used in tier 2 under the identical protocol (Guerreiro Stucklin et al., 2019).

NanoString nCounter Vantage 3D for Protein Analysis

RNA and protein were simultaneously analyzed on the NanoString nCounter system. RNA in addition to one slide (10 μm) of FFPE was used for protein analysis. Samples were deparaffinized, processed according to the NanoString protocol and incubated with the antibodies of interest overnight. The RNA (50-100 ng) and the protein lysate were hybridized with the TagSet for 16-24 h at 67°C and loaded on the nCounter Prep Station, where each DNA oligonucleotide is UV cleaved and recognized by a unique reporter probe that contains a fluorescent barcode. All analytes are imaged and counted simultaneously by the nCounter Analysis System to provide a direct, digital readout of RNA, and protein expression in tandem.

Fluorescent In Situ Hybridization

Fluorescent *in situ* hybridization was designed to detect *BRAF*, *MYB*, *MYBL1*, and *FGFR2* fused transcripts by using bacterial artificial chromosome clones located over each respective gene target. Probes were obtained from The Center for Applied Genomics (HSC, Toronto, Canada) and are available upon request. Clones were directly labeled with Spectrum Green or Spectrum Orange fluorochrome. Paraffin fluorescent *in situ* hybridization analysis was performed on 4-μm tumor sections. Slides were baked overnight to fix the section to the slide and were pretreated by using a paraffin pretreatment kit (Abbott, Chicago IL). Sections were dehydrated before slide/probe co-denaturation on thermobrite (Intermedico, Markham, ON, Canada). Denaturation conditions used for paraffin-embedded slides/probes were as follows:

1. 85°C for 7 min
2. 37°C overnight

Slides were washed in ×0.4 side scatter/0.3% NP-40 at 73°C for 30 s, followed by ×2 side scatter/0.1% NP-40 at room temperature for 30 s. Slides were counterstained with DAPI. Nuclei were analyzed by using an Axioplan2 epifluorescence microscope (Zeiss, Jena, Germany). Images were captured by an Axiocam MRm Camera (Imaging Associates, Bicester, United Kingdom) and analyzed by using an imaging system with Isis Software (Version 5.1.110; MetaSystems, Boston, MA).

Immunohistochemistry

Detection of BRAF p.V600E and H3.3 p.K27M by immunohistochemistry was performed on a Benchmark Ventana Machine (Tucson, AZ) using the Optiview detection kit (Tucson, AZ). CC1 was used for heat retrieval for 40 min and slides were incubated for 36 min with the respective target antibody. Antibodies used were as follows:

1. Mouse Anti-Human BRAF p.V600E Monoclonal Antibody from Spring Bioscience (E19290, Pleasanton, CA).
2. Rabbit Anti-Histone H3F3A p.K27M Polyclonal Antibody from Millipore (ABE419, Burlington, MA)

Casein was used for 8 min to help lessen background staining and haematoxylin counterstain was used for 12 min.

SNP Array

Samples were hybridized to the Genome-Wide Human SNP Array 6.0 from Affymetrix (Santa Clara, CA, USA). The sample preparation, including DNA extraction, digestion, labelling and hybridization, was performed as directed by the manufacturer. Data were analyzed using Partek Genomics Suite v6.4 (Partek Incorporated, St. Louis, MO, and Genotyping Console 4.1 (Affymetrix), GISTIC2.0 (Broad Institute, Cambridge, MA, USA).

Targeted DNA Sequencing

Samples with sufficient material and negative for our targeted testing protocol had their DNA constructed into DNA-sequencing libraries using the Illumina Ampliseq Comprehensive DNA Focus Panel Kit (Illumina, San Diego, CA), following the manufacturer's guidelines utilizing the Illumina Library PLUS Kit (Illumina, San Diego, CA). Sequencing adapters were ligated to the fragments to allow for amplification of the DNA followed by a quality control validation step to ensure proper adapter ligation. Samples were next hybridized to Ampliseq CD indexes (Illumina, San Diego, CA) used to enrich for 52 cancer-associated genes outlined in the manufacturer's documentation prior to amplification. Paired-end DNA-sequencing was performed using the Illumina MiSeq sequencing platform and the MiSeq Reagent Micro Kit V2 (Illumina, San Diego, CA). Raw sequencing data was converted to the fastq format and analyzed using the BaseSpace application (Illumina, San Diego, CA), with DNA-Seq Alignment V.1.0.0. Variant calling was completed in BaseSpace using the Isaac Variant Caller.

Whole Transcriptome Sequencing

Samples with sufficient RNA quality and quantity were sent for whole transcriptome sequencing at The Center for Applied Genomic (HSC, Toronto, Canada). Library preparation was completed using the TruSeq RNA Library Prep Kit v2 (Illumina, San Diego, CA) using the rRNA depletion kit RiboZero Gold (Illumina, San Diego, CA) according to the manufacturer's specifications. Paired-end sequencing was performed on the Illumina HiSeq 2500 platform to an average of 250 million paired reads. STAR (Dobin et al., 2013) was used to align the raw sequencing data to genome reference 'Homo sapiens UCSC hg19' (RefSeq and Gencode gene annotations). Fusion events were independently called using 4 fusion callers:

1. DeFuse (McPherson et al., 2011)
2. TopHat (Kim and Salzberg, 2011)
3. Ericscript (Benelli et al., 2012)
4. FusionMap (Ge et al., 2011)

Variant calling from RNAseq was completed using Annovar (Wang et al., 2010).

Gene Set Enrichment Analysis

Gene expression was counted with HTSeq (Anders et al., 2015), and differential expression calculated with edgeR (Robinson et al., 2010). Genes were ranked by multiplying their fold-change sign with the -log10 (adjusted p value) for pre-ranked GSEA (Subramanian et al., 2005). For ssGSEA, reads were aligned to the transcriptome using RSEM-v1.2 (Li and Dewey, 2011). Genes with mean FPKM < 1 were discarded, and genes with duplicated names were filtered to keep the most expressed gene.

Genetic Analysis at Collaborating Institutions

Molecular analysis of supplemental cases provided from our collaborators were determined based on institute-specific protocols (Surrey et al., 2019; Cheng et al., 2015; Rusch et al., 2018). The details of these protocols are available upon request.

QUANTIFICATION AND STATISTICAL ANALYSIS

Statistical analysis was carried out using a combination of R 3.3.1 (www.r-project.org), GraphPad Prism version 7.00 for Windows (La Jolla California USA, www.graphpad.com), and IBM SPSS Statistics for Windows, Version 25.0. (Armonk, NY: IBM Corp). Categorical comparisons of counts were carried out using Fisher's exact test, comparisons between groups of continuous variables were completed using a Student's t-test, Wilcoxon signed–rank test, ANOVA or Mann-Whitney U test (specified in the text). Differences in survival were analysed by the Kaplan-Meier method and significance determined by the log-rank test. Univariate and multivariate analysis was done using multivariate Cox proportional hazards models and significance testing (α=0.05) based on the Wald test. All tests were two-sided and a p value of less than 0.05 was considered significant.

DATA AND CODE AVAILABILITY

RNAseq data sets and Ampliseq DNA sequencing have been deposited in the European-Genome-Phenome Archive: EGAS00001004242. Additional data not infringing on ethics restrictions is available upon request to the corresponding authors.

Cancer Cell, Volume *37*

Supplemental Information

Integrated Molecular and Clinical Analysis of 1,000 Pediatric Low-Grade Gliomas

Scott Ryall, Michal Zapotocky, Kohei Fukuoka, Liana Nobre, Ana Guerreiro Stucklin, Julie Bennett, Robert Siddaway, Christopher Li, Sanja Pajovic, Anthony Arnoldo, Paul E. Kowalski, Monique Johnson, Javal Sheth, Alvaro Lassaletta, Ruth G. Tatevossian, Wilda Orisme, Ibrahim Qaddoumi, Lea F. Surrey, Marilyn M. Li, Angela J. Waanders, Stephen Gilheeney, Marc Rosenblum, Tejus Bale, Derek S. Tsang, Normand Laperriere, Abhaya Kulkarni, George M. Ibrahim, James Drake, Peter Dirks, Michael D. Taylor, James T. Rutka, Suzanne Laughlin, Manohar Shroff, Mary Shago, Lili-Naz Hazrati, Colleen D'Arcy, Vijay Ramaswamy, Ute Bartels, Annie Huang, Eric Bouffet, Matthias A. Karajannis, Mariarita Santi, David W. Ellison, Uri Tabori, and Cynthia Hawkins

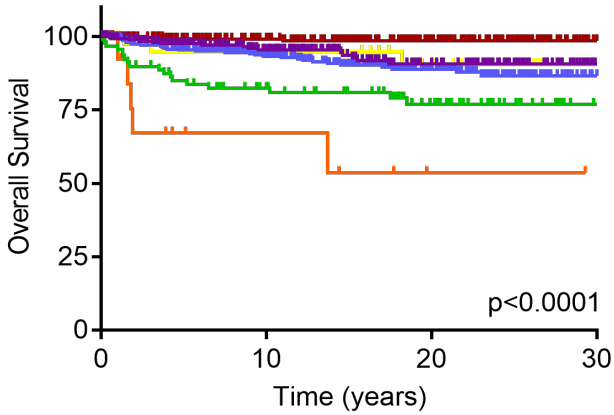

Number at Risk				
Hemispheres	265	158	75	9
Diencephalon	313	213	103	10
Brainstem	92	56	35	3
Cerebellum	252	182	101	13
Spine	41	29	19	3
Disseminated	13	6	2	1

Figure S1. Additional Cohort Details, Related to Figure 1.
Overall survival of the pLGG cohort segrgated by tumor location. p value calculated via the log-rank test.

Table S2. Clinicopathologic characteristics of NF1-driven pLGG, related to Figure 2

Number		
	N	133
Pathology		
	PA	10
	GG	4
	PXA	0
	LGG, NOS	7
	DA	3
	ODG	0
	DNET	1
	GNT	0
	AG	0
	DIA/DIG	0
	Not Biopsied	108
Location		
	Hemispheres	2
	Diencephalon	124
	Brainstem	4
	Cerebellum	1
	Spine	1
	Disseminated	1
Age at Diagnosis		
	Mean	6.0 ± 4.0 years
	Median	4.7 (0.5-17.1) years
Sex		
	Male	75
	Female	58
Progression		
	Progressed	35
	Stable	97
	Unknown	1
	5-year PFS	79.8%
	10-year PFS	72.5%
Outcome		
	Dead	4
	Alive	129
	5-year OS	99.2%
	10-year OS	99.2%

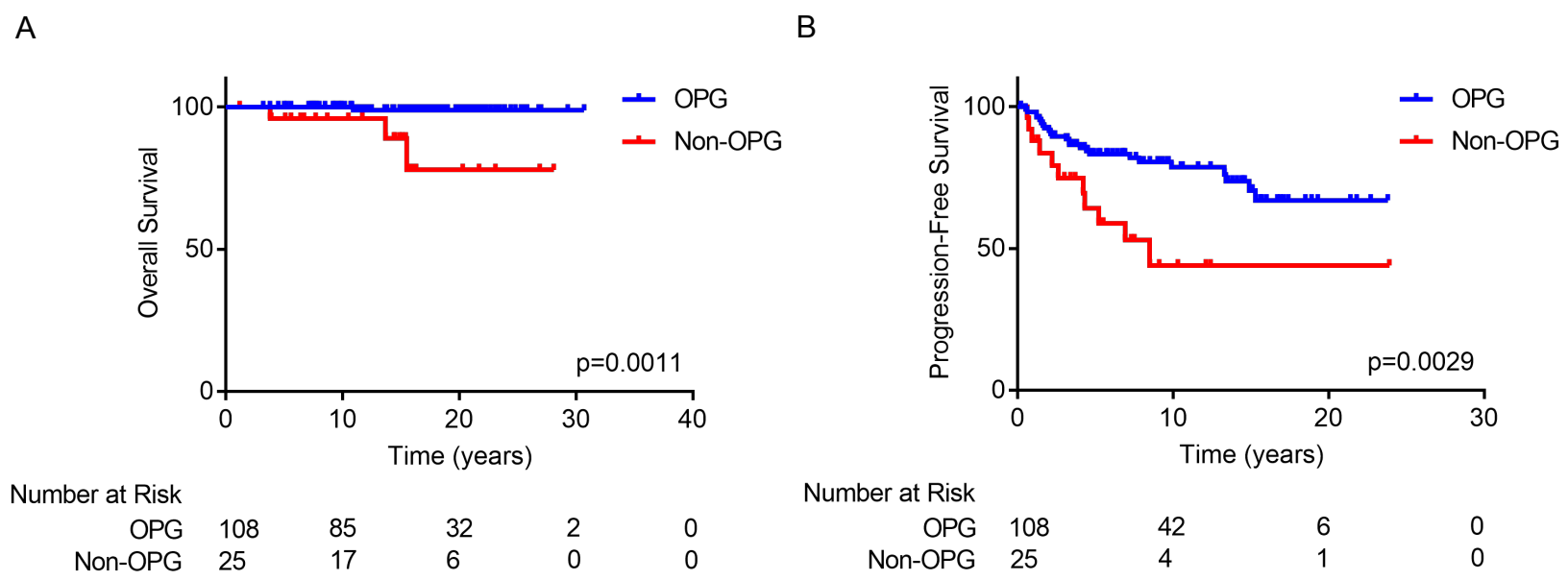

Figure S2. Survival of NF1 altered pLGG, related to Figure 2.

(A) Kaplan-Meier plot of overall survival of cases separated by NF1 tumors occurring within the optic pathway (OPG) versus those outside of the optic pathway. p value calculated via the log-rank test.

(B) Kaplan-Meier plot of progression-free survival of cases separated by NF1 tumors occurring within the optic pathway (OPG) versus those outside of the optic pathway. p value calculated via the log-rank test.

A

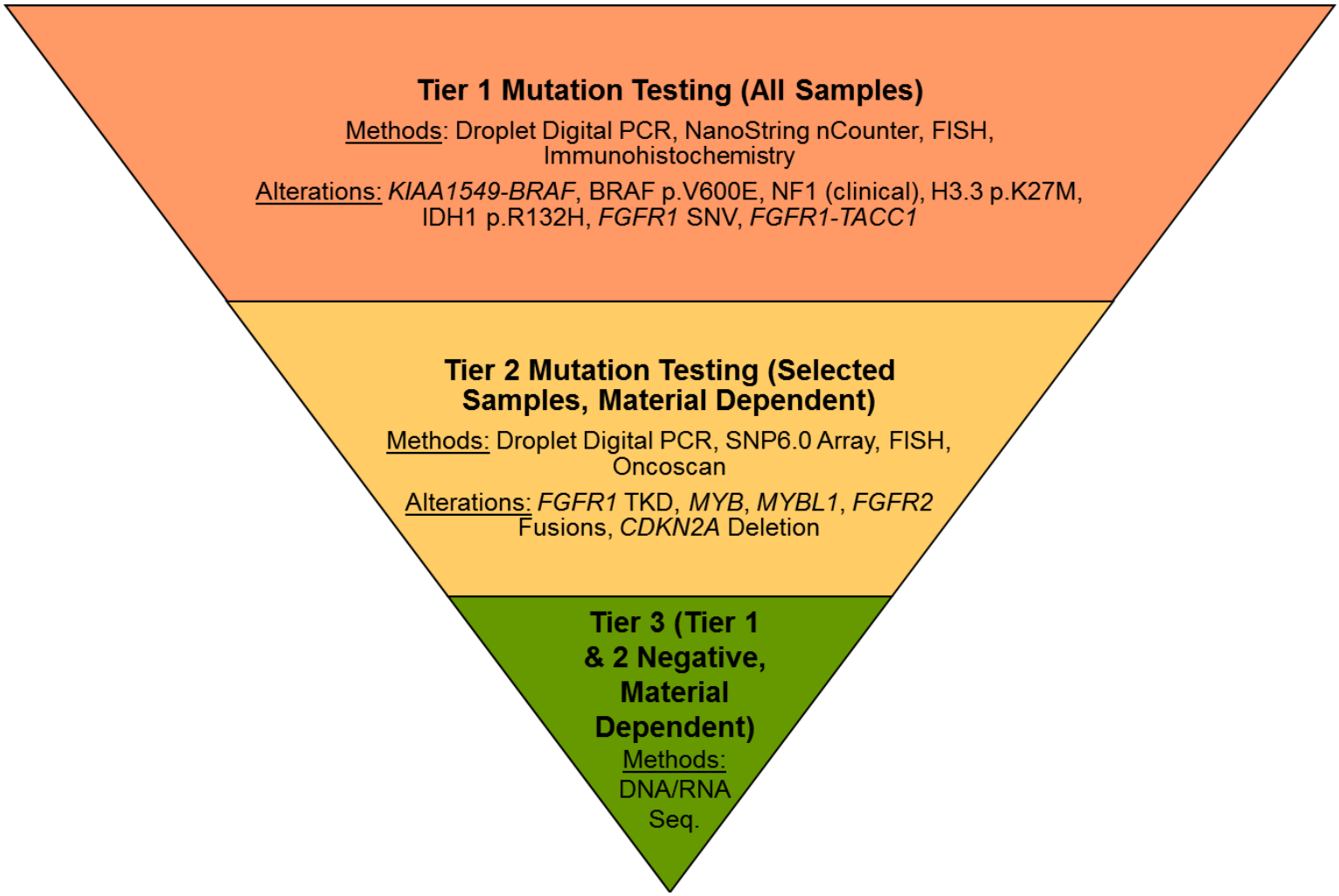

B

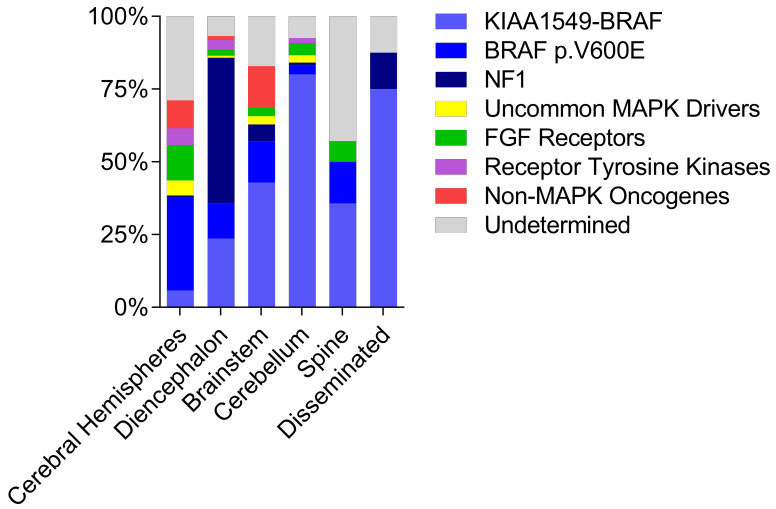

C

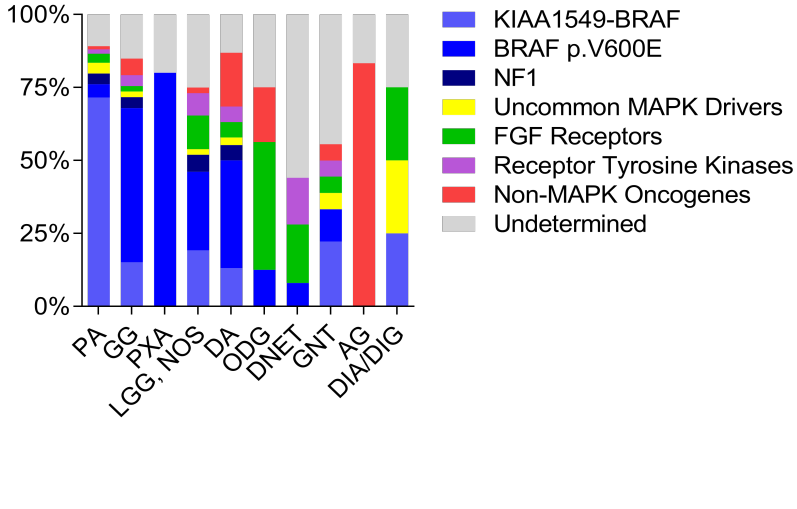

Figure S3. Additional Molecular Details, related to Figure 2

(A) Tiered molecular characterization pipeline utilized in this report. Limitations of sample availability and quality dictated the extent of characterization per sample.

(B) Frequency of molecular alterations across anatomical tumor location.

(C) Frequency of molecular alterations across tumor histology.

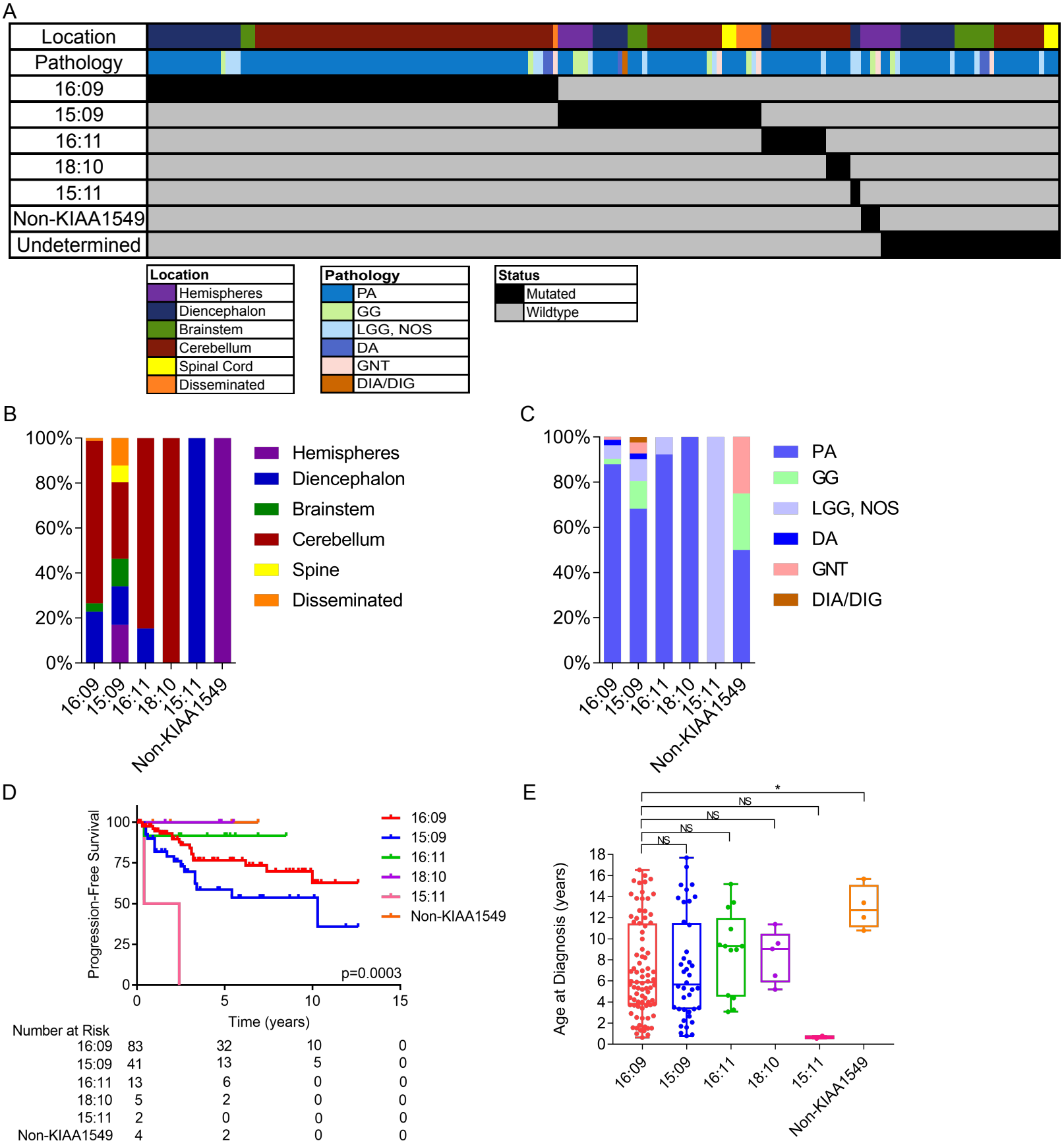

Figure S4. Clinical and genomic characteristics of *KIAA1549-BRAF* pLGG, related to Figure 5

(A) Oncoprint representation of the *BRAF* fusion breakpoints (n=184). Samples are arranged in columns with ifusion subtypes labelled along the row.

(B) Anatomical location of *BRAF* fused pLGG based on their fusion breakpoint and/or fusion partner

(C) Histological diagnosis of *BRAF* fused pLGG based on their fusion breakpoint and/or fusion partner

(D) Kaplan-Meier plot of progression-free survival of cases separated by breakpoint and/or fusion partner. p value calculated via the log-rank test.

(E) Boxplot showing the age of diangosis of *BRAF* fused patient separated by breakpoint and/or fusion partner. The thick line within the box represents the median, the lower and upper limits of the box represent the first and third quartiles, and the whiskers the min. and max. Adjusted p value for all pairwise comparisons, t-test. *<0.05

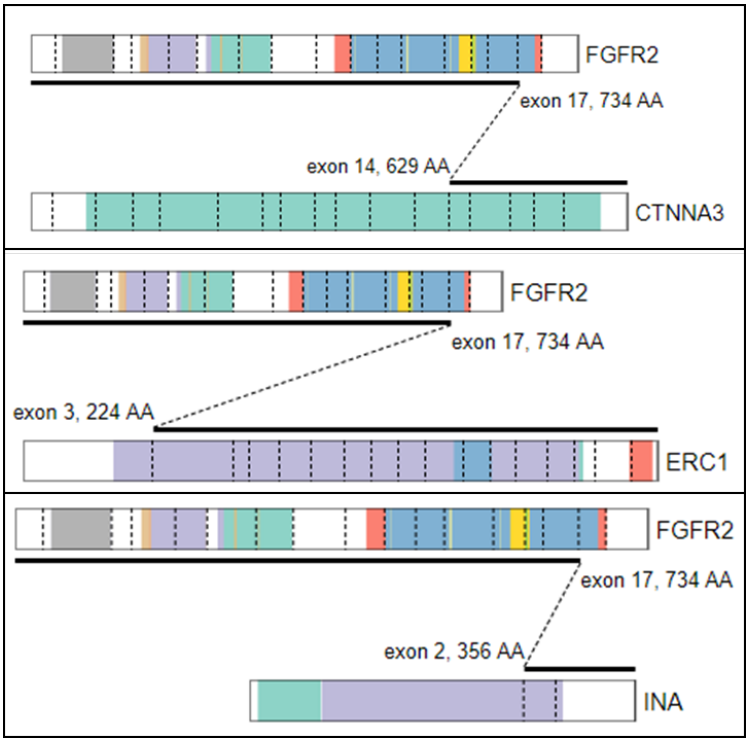

Figure S5. *FGFR2* fusions identified in pLGG, related to Figure 5

Schematic representation of the *FGFR2* fusions identified in this study. Figures were derived using the Protein Paint feature of the St. Jude Pecan website (http://pecan.stjude.cloud/proteinpaint)

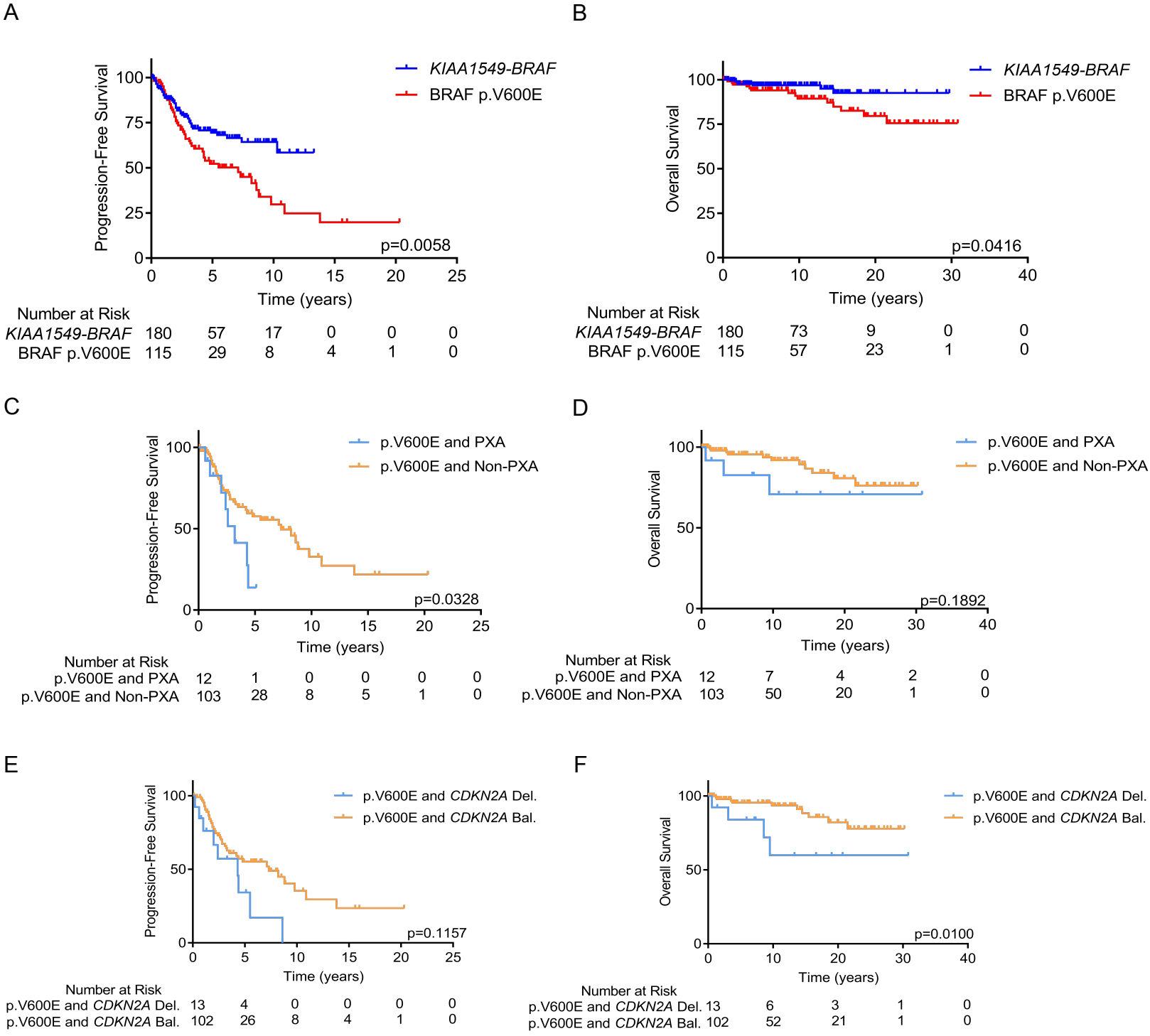

Figure S6. Survival of *BRAF* altered pLGG, related to Figure 6

(A) Kaplan-Meier plot of progression-free survival of *KIAA1549-BRAF* versus BRAF p.V600E cases. p value calculated via the log-rank test.

(B) Kaplan-Meier plot of overall survival of *KIAA1549-BRAF* versus BRAF p.V600E cases. p value calculated via the log-rank test.

(C) Kaplan-Meier plot of progression-free survival of cases separated by BRAF p.V600E occurring in pleomorphic xanthoastrocytoma versus not. p value calculated via the log-rank test.

(D) Kaplan-Meier plot of overall survival of cases separated by BRAF p.V600E occurring in pleomorphic xanthoastrocytoma versus not. p value calculated via the log-rank test.

(E) Kaplan-Meier plot of progression-free survival of cases separated by BRAF p.V600E occurring with *CDKN2A* deletion versus balanced *CDKN2A*. p value calculated via the log-rank test.

(F) Kaplan-Meier plot of overall survival of cases separated by BRAF p.V600E occurring with *CDKN2A* deletion versus balanced *CDKN2A*. p value calculated via the log-rank test.

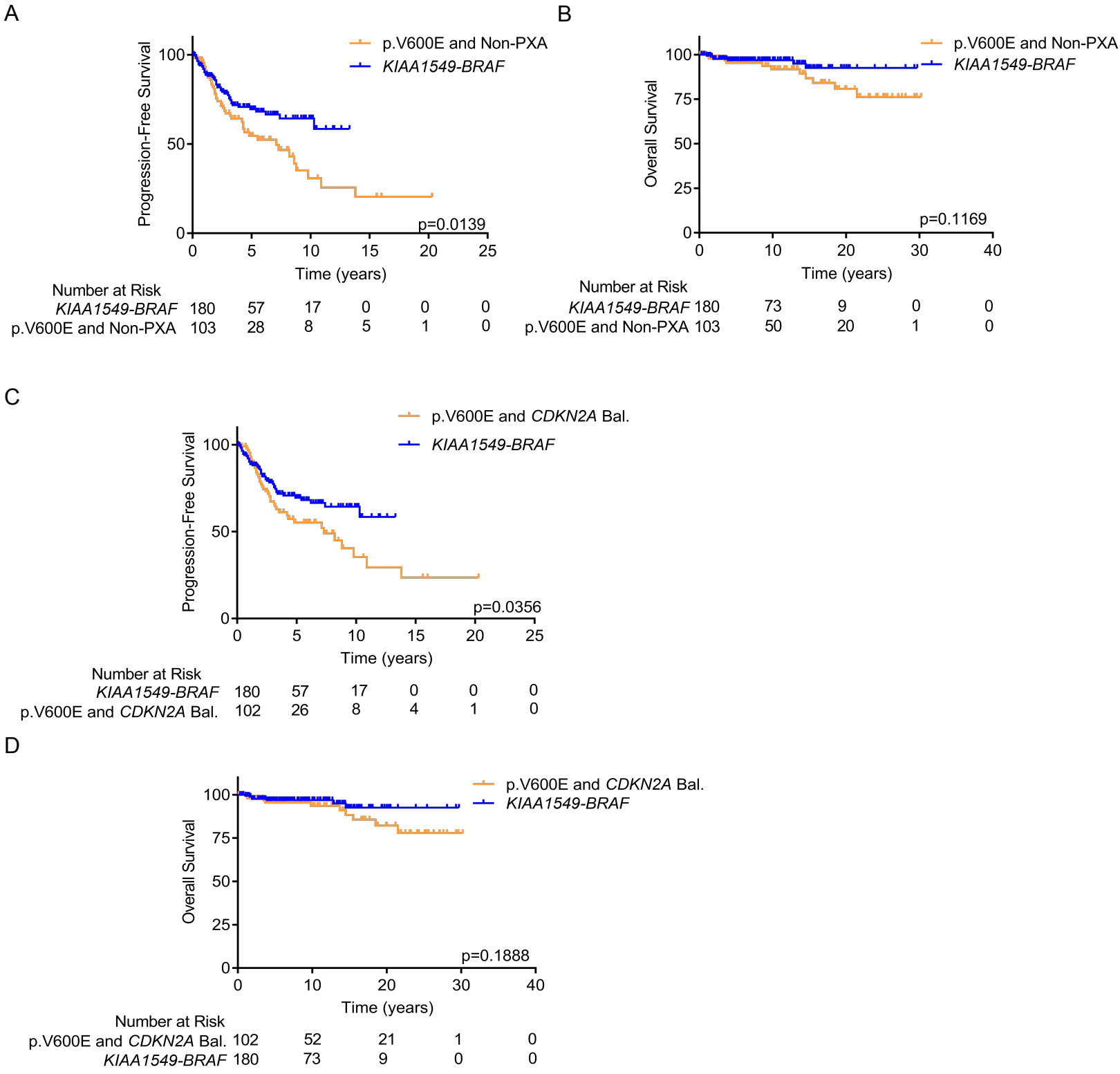

Figure S7. Survival of low risk BRAF p.V600E versus *KIAA1549-BRAF* altered pLGG, related to Figure 6.
(A) Kaplan-Meier plot of progression-free survival of cases separated by BRAF p.V600E without pleomorphic xanthoastrocytoma versus *KIAA1549-BRAF*. p value calculated via the log-rank test.
(B) Kaplan-Meier plot of overall survival of cases separated by BRAF p.V600E without pleomorphic xanthoastrocytoma versus *KIAA1549-BRAF*. p value calculatd via the log-rank test.
(C) Kaplan-Meier plot of progression-free survival of cases separated by BRAF p.V600E without *CDKN2A* deletion versus *KIAA1549-BRAF*. p value calculated via the log-rank test.
(D) Kaplan-Meier plot of overall survival of cases separated by BRAF p.V600E without *CDKN2A* deletion versus *KIAA1549-BRAF*. p value calculated via the log-rank test.

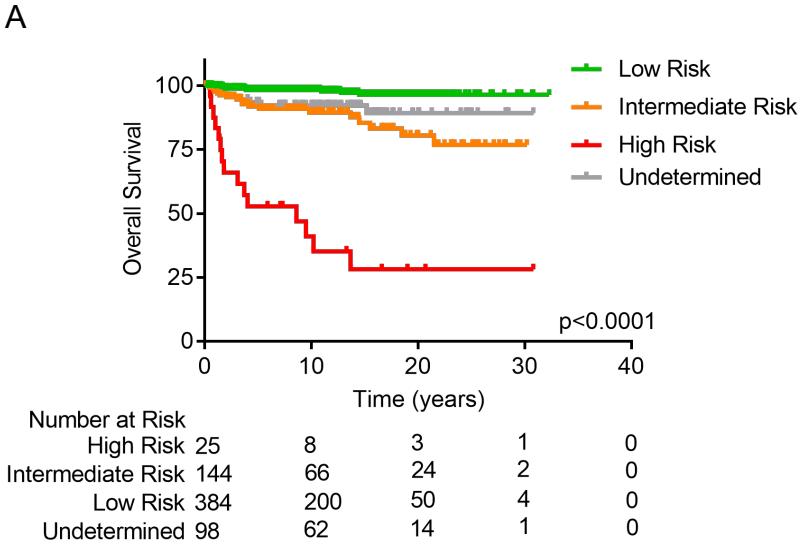

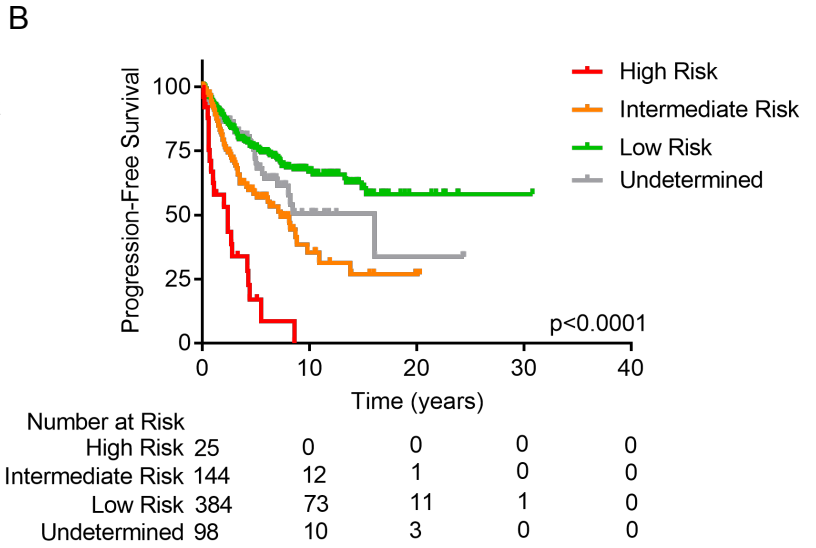

Figure S8. Risk stratification of pLGG including samples without an associated molecular risk, related to Figure 7.
(A) Kaplan-Meier plot of overall survival of cases separated by their assigned risk, including those with. undetermined risk. p value calculated via the log-rank test. .
(B) Kaplan-Meier plot of progression-free survival of cases separated by their assigned risk, including those with. undetermined risk. p value calculated via the log-rank test. .

Table S5. Univariate and multivariate Cox proportional hazard analysis of pLGG for predictors of tumor progression, related to Figure 7.

Variable	**Univariate**			**Multivariate**		
Progression	|HR|	95% C.I.	p-value	|HR|	95% C.I.	p-value
Age at Diagnosis	0.997	0.943-1.011	0.180	0.947	0.904-0.993	0.023
Tumor Location (Midline)	1.266	0.901-1.778	0.174	1.621	0.924-2.843	0.092
Sex (Male)	0.855	0.632-1.157	0.310	0.817	0.542-1.232	0.334
Extent of Resection (GTR)	0.302	0.199-0.460	<0.0001	0.345	0.198-0.601	<0.0001
Histological Grade (grade II)	1.565	1.030-2.377	0.036	1.353	0.760-2.408	0.305
Histology Type (PA)	1.083	0.786-1.491	0.627	1.035	0.567-1.888	0.912
Alteration Type (SNV)	1.986	1.420-2.778	<0.0001	N/A	N/A	N/A
Risk Stratification (Low)			0.000			0.000
Risk Stratification (Intermediate)	2.087	1.493-2.918	<0.0001	1.513	0.973-2.352	0.046
Risk Stratification (High)	6.523	3.989-10.667	<0.0001	4.030	2.030-7.998	<0.0001
Death	|HR|	95% C.I.	p-value	|HR|	95% C.I.	p-value
Age at Diagnosis	1.014	0.944-1.089	0.702	0.960	0.868-1.062	0.432
Tumor Location (Midline)	0.893	0.428-1.865	0.764	1.753	0.639-4.806	0.275
Sex (Male)	1.399	0.696-2.813	0.346	0.453	0.175-1.171	0.102
Extent of Resection (GTR)	0.280	0.098-0.802	0.018	0.140	0.035-0.561	0.005
Histological Grade (grade II)	4.152	1.972-8.745	<0.0001	1.572	0.530-4.657	0.415
Histology Type (PA)	0.419	0.173-1.017	0.055	0.271	0.072-1.025	0.054
Alteration Type (SNV)	4.755	2.041-11.075	<0.0001	N/A	N/A	N/A
Risk Stratification (Low)			0.000			0.000
Risk Stratification (Intermediate)	2.804	1.111-7.076	0.029	1.694	0.506-5.671	0.392
Risk Stratification (High)	38.681	16.876-88.657	<0.0001	16.547	4.556-59.958	<0.0001